

**Equation-of-state-dependent surface free-energy density for wettability in lattice Boltzmann method**Rongzong Huang ,\* Hao Yang, and Yueyan Xing*School of Energy Science and Engineering, Central South University, Changsha 410083, China* (Received 1 September 2022; revised 6 December 2022; accepted 5 February 2023; published 27 February 2023)

In thermodynamic theory, the liquid-vapor fluids can be described by a single multiphase equation of state and the surface wettability is usually characterized by the surface free-energy density. In this work, we propose an equation-of-state-dependent surface free-energy density for the wettability of the liquid-vapor fluids on a solid surface, which can lead to a simple closed-form analytical expression for the contact angle. Meanwhile, the thermodynamically derived equilibrium condition is equivalent to the geometric formulation of the contact angle. To numerically validate the present surface free-energy density, the mesoscopic multiphase lattice Boltzmann model with self-tuning equation of state, which is strictly consistent with thermodynamic theory, is employed, and the two-dimensional wetting condition treatment is extended to the three-dimensional situation with flat and curved surfaces. Two- and three-dimensional lattice Boltzmann simulations of static droplets on flat and curved surfaces are first performed, and the obtained contact angles agree well with the closed-form analytical expression. Then, the three-dimensional lattice Boltzmann simulation of a moving droplet on an inclined wall, which is vertically and sinusoidally oscillated, is carried out. The dynamic contact angles well satisfy the Cox-Voinov law. The droplet movement regimes are consistent with previous experiments and two-dimensional simulations. The dependence of the droplet overall velocity with respect to the dimensionless oscillation strength is also discussed in detail.

DOI: [10.1103/PhysRevE.107.025309](https://doi.org/10.1103/PhysRevE.107.025309)**I. INTRODUCTION**

Multiphase flows are widely encountered in daily life and are of great importance in lots of engineering applications. In most applications, the solid surface is involved, and the surface wettability could even dominate the dynamics of multiphase flows. Related problems include digital microfluidics, capillary rise, nucleate boiling, dropwise condensation, etc. The development of the phase interface and the nonzero surface tension along the phase interface make numerically modeling multiphase flows a challenging task. Once the solid surface is involved, the dynamics of the three-phase contact line further increase the difficulty in numerically modeling such problems. Physically speaking, the dynamics of multiphase flows and surface wettability are the natural consequences of the underlying microscopic molecular interaction, which is relatively simple compared with the complex and diverse macroscopic mechanisms. As a mesoscopic method that originates from the lattice gas automata, the lattice Boltzmann (LB) method has the potential to incorporate microscopic interaction and thus has been widely applied to numerically modeling multiphase flows over the past three decades [1–6].

In thermodynamic theory, the liquid-vapor fluids, like water and steam, can be described by a single multiphase equation of state (EOS), and the liquid-vapor phase interface is diffusive rather than sharp, which means the density across the phase interface varies continuously rather than as a step function [7]. With such a diffusive phase interface, the

nonzero surface tension naturally arises [7] and the viscous singularity at the moving contact line can also be naturally circumvented [8]. In addition, the wettability of the liquid-vapor fluids on a solid surface is usually characterized by the surface free-energy density [9]. All the existing multiphase LB models, including the widely applied pseudopotential and free-energy LB models, are based on the diffusive phase interface. The pseudopotential LB model is originally proposed by Shan and Chen in 1993 [2], where a pairwise interaction force is introduced to mimic the underlying microscopic interaction responsible for multiphase flows. Due to its simplicity in concept and computation, the pseudopotential LB model has attracted continuous attention and significant progress has been made [10–12]. Shan [10] analyzed the origin of the spurious current and then proposed a general method to reduce the magnitude and extent of the spurious current. Sbragaglia *et al.* [11] proposed a multirange pseudopotential LB model that allows independently tuning the multiphase EOS and surface tension. Li *et al.* [12] analyzed various schemes to incorporate the force term into the LB equation and found the mechanism to adjust the coexistence densities close to the thermodynamic results. The free-energy LB model is originally proposed by Swift *et al.* in 1995 [3], where the pressure tensor in thermodynamic theory is directly employed to describe multiphase flows, implying that thermodynamic consistency can be ensured in advance. Significant progress has been made to restore the Galilean invariance [13], increase the density ratio [14], and reduce the spurious current [15]. In 2019, Huang *et al.* [16] proposed the multiphase LB model with self-tuning EOS by handling the microscopic molecular interaction. The short-range repulsive and long-range

\*Corresponding author: [rongzong.huang@csu.edu.cn](mailto:rongzong.huang@csu.edu.cn)

attractive molecular interactions are handled by recovering a self-tuning EOS via the collision operator and incorporating a pairwise interaction force via the force term, respectively, which makes this multiphase LB model complies with the thermodynamic foundations of kinetic theory [17] and thus be strictly consistent with thermodynamic theory [16].

In the pseudopotential LB model, various schemes have been proposed for the surface wettability [18–21]. Particularly, Benzi *et al.* [19] introduced a wall density to fix the pseudopotential inside the wall, which is then used to calculate the pairwise interaction force on the wall node. They further derived an analytical expression for the contact angle and found that the contact angle can be effectively adjusted by tuning the wall density. In Benzi *et al.*'s work [19], the exponential pseudopotential is used to calculate the pairwise interaction force, implying that the considered multiphase EOS is a specific one, and the Shan-Chen's scheme is adopted to incorporate the pairwise interaction force into the LB equation. Nevertheless, it is difficult, if not impossible, to connect the surface wettability in the pseudopotential LB model with the surface free-energy density in thermodynamic theory because the model suffers from thermodynamic inconsistency [17], although equivalent theories can be formulated for this model to analytically determine thermodynamical properties like the coexistence densities and surface tension [11, 19, 22]. In the free-energy LB model, Briant *et al.* [23, 24] first studied the surface wettability by using the surface free-energy density in linear form, which is proposed by Cahn [25] for critical point wetting. They derived a closed-form analytical expression for the contact angle when the Landau free-energy functional is employed for the bulk phases (the liquid-vapor fluids). The linear surface free-energy density has also been used by Semperebon *et al.* [26] in the ternary free-energy LB model. Most recently, Huang *et al.* [27] proposed a surface free-energy density in hyperbolic tangent form and derived the analytical expression for the contact angle when a general multiphase EOS is employed. They further investigated the wetting condition treatment, though two-dimensional, in the multiphase LB model with self-tuning EOS, which gathers the distinct advantages of the pseudopotential and free-energy LB models.

It is worth noting that, in physics, the surface wettability depends on not only the physicochemical properties of the solid surface but also the thermodynamical properties of the liquid-vapor fluids. Therefore, the surface free-energy density for wettability is expected to be explicitly related to the multiphase EOS, while the existing surface free-energy densities, such as the linear one [25] and the hyperbolic tangent one [27], are proposed without considering any details of the multiphase EOS. Moreover, when a realistic multiphase EOS is employed, the analytical expressions for the contact angle derived with the existing EOS-independent surface free-energy densities are very complicated, as shown by Huang *et al.* [27]. In this work, we will thermodynamically analyze the wettability of the liquid-vapor fluids on a solid surface when the multiphase EOS can be arbitrarily specified, and then we will propose an EOS-dependent surface free-energy density for wettability, which leads to a simple closed-form analytical expression for the contact angle that is convenient for numerical implementation. The existing wetting condition

treatment in the multiphase LB model with self-tuning EOS will also be extended to the three-dimensional situation with flat and curved surfaces. The remainder of this work is organized as follows. In Sec. II, the thermodynamic analysis of surface wettability is made and the EOS-dependent surface free-energy density is proposed. In Sec. III, the multiphase LB model with self-tuning EOS is introduced and the wetting condition treatment is proposed. The numerical validations are performed in Sec. IV and a brief conclusion is presented in Sec. V.

## II. THERMODYNAMIC THEORY

For a liquid-vapor system surrounded by a solid surface, the Helmholtz free-energy functional  $\mathcal{F}$  can be written as [7]

$$\mathcal{F} = \int_{\Omega} \left( \rho f_b + \frac{1}{2} \kappa |\nabla \rho|^2 \right) dV + \int_{\partial\Omega} \rho f_s dA, \quad (1)$$

where  $\Omega$  and  $\partial\Omega$  denote the material volume and its surface (i.e., the solid surface), respectively,  $\rho f_b$  is the bulk free-energy density with  $\rho$  the fluid density and  $f_b$  the specific bulk free energy, respectively,  $\frac{1}{2} \kappa |\nabla \rho|^2$  is the interface free-energy density for the liquid-vapor phase interface with  $\kappa$  the excess energy coefficient, and  $\rho f_s$  is the surface free-energy density (per unit area) for the solid surface. The equilibrium state of the liquid-vapor system can be obtained by minimizing the Helmholtz free-energy functional under the constraint of mass conservation. For this purpose, the following functional  $\mathcal{W}$  is introduced:

$$\mathcal{W} = \mathcal{F} + \lambda \mathcal{M}, \quad (2a)$$

where  $\mathcal{M} = \int_{\Omega} \rho dV$  is the total mass and  $\lambda$  is the Lagrange multiplier. The first variation of  $\mathcal{W}$  is

$$\begin{aligned} \delta \mathcal{W} = & \int_{\Omega} \delta \rho \left[ \frac{\partial(\rho f_b)}{\partial \rho} - \kappa \nabla \cdot \nabla \rho + \lambda \right] dV \\ & + \int_{\partial\Omega} \delta \rho \left[ \kappa \nabla \rho \cdot \hat{\mathbf{n}}_s + \frac{\partial(\rho f_s)}{\partial \rho} \right] dA, \end{aligned} \quad (2b)$$

where  $\hat{\mathbf{n}}_s$  is the outward unit normal vector of the solid surface. Minimizing  $\mathcal{W}$  with respect to  $\rho$ , the equilibrium conditions of the liquid-vapor system can be obtained from Eq. (2b) as follows:

$$\frac{\partial(\rho f_b)}{\partial \rho} - \kappa \nabla \cdot \nabla \rho = -\lambda \equiv \text{const} \quad \text{in } \Omega, \quad (3a)$$

$$\kappa \nabla \rho \cdot \hat{\mathbf{n}}_s + \frac{\partial(\rho f_s)}{\partial \rho} = 0 \quad \text{on } \partial\Omega. \quad (3b)$$

Note that an athermal multiphase system is considered here, and thus the isothermal equilibrium condition is inherently implied.

Based on the form of Eq. (3a), a pressure tensor  $\mathbf{P}$  can be defined as

$$\nabla \cdot \mathbf{P} \equiv \rho \nabla \left[ \frac{\partial(\rho f_b)}{\partial \rho} - \kappa \nabla \cdot \nabla \rho \right], \quad (4)$$

and then calculated as

$$\mathbf{P} = \left( \rho^2 \frac{\partial f_b}{\partial \rho} - \kappa \rho \nabla \cdot \nabla \rho - \frac{\kappa}{2} \nabla \rho \cdot \nabla \rho \right) \mathbf{I} + \kappa \nabla \rho \nabla \rho. \quad (5)$$

The quantity  $\partial(\rho f_b)/\partial\rho - \kappa\nabla \cdot \nabla\rho$  on the right-hand side of Eq. (4) is identified as the chemical potential in previous works [15,27,28], although it is not strictly the local one in the theory of van der Waals [7,29,30]. In addition, there is an infinite number of pressure tensors satisfying Eq. (4), which differ by symmetric tensors with vanishing divergence, and the Korteweg's stress tensor is adopted [31]. With the definition of the pressure tensor, the equilibrium condition given by Eq. (3a) also reads

$$\nabla \cdot \mathbf{P} = \mathbf{0} \quad \text{in } \Omega. \quad (6)$$

In thermodynamic theory, the specific bulk free energy  $f_b$ , with natural variables the specific volume  $v$  ( $v \equiv \rho^{-1}$ ) and the temperature  $T$ , can be chosen as a characteristic function (thermodynamic potential), and then the thermodynamic pressure  $p_{\text{EOS}}$  can be defined as

$$p_{\text{EOS}} \equiv -\left(\frac{\partial f_b}{\partial v}\right)_T = \rho^2 \left(\frac{\partial f_b}{\partial \rho}\right)_T. \quad (7)$$

In real applications, the thermodynamic pressure  $p_{\text{EOS}}$  is usually given via the multiphase EOS  $p_{\text{EOS}}(\rho, T)$ , and the expression for the specific bulk free energy  $f_b$  could be unknown.

### A. Thermodynamic properties

To theoretically calculate the thermodynamic properties (including the saturated liquid and vapor densities, the saturation pressure, the contact angle, etc.), a one-dimensional system can be taken for simplicity, where both the liquid-vapor phase interface and the solid surfaces are parallel to the  $y$ - $z$  plane and all the involved quantities only vary with the  $x$  coordinate [27]. For such a one-dimensional system, the pressure tensor given by Eq. (5) can be simplified as

$$\begin{aligned} P_n \equiv P_{xx} &= p_{\text{EOS}} - \kappa\rho \frac{d^2\rho}{dx^2} + \frac{\kappa}{2} \left(\frac{d\rho}{dx}\right)^2 \\ &= p_{\text{EOS}} + \frac{\kappa}{2} \frac{d}{dv} \left[ \frac{1}{\rho} \left(\frac{d\rho}{dx}\right)^2 \right], \end{aligned} \quad (8a)$$

$$P_t \equiv P_{yy} = P_{zz} = p_{\text{EOS}} - \kappa\rho \frac{d^2\rho}{dx^2} - \frac{\kappa}{2} \left(\frac{d\rho}{dx}\right)^2, \quad (8b)$$

$$P_{\alpha\beta} = 0 \quad \text{if } \alpha \neq \beta, \quad (8c)$$

where  $P_n$  and  $P_t$  denote the normal and tangential pressures, respectively. The equilibrium condition given by Eq. (6) indicates that  $P_n$  should keep constant in  $\Omega$ . Therefore, we have

$$P_n = p_{\text{EOS}}(\rho_l) = p_{\text{EOS}}(\rho_v) = p_{\text{sat}}, \quad (9)$$

considering  $d\rho/dx = 0$  and  $d^2\rho/dx^2 = 0$  in the bulk liquid and vapor phases. Here,  $\rho_l$  and  $\rho_v$  are the saturated liquid

and vapor densities, respectively, and  $p_{\text{sat}}$  is the saturation pressure.

With Eq. (9), an indefinite integral of Eq. (8a) can be derived as

$$\frac{\kappa}{2} \left(\frac{d\rho}{dx}\right)^2 = \rho \left[ \int (p_{\text{sat}} - p_{\text{EOS}}) dv + C \right] = p_{\text{sat}} - \rho\Theta + \rho C, \quad (10)$$

where  $\Theta = \int p_{\text{EOS}} dv$  is the indefinite integral of the multiphase EOS, and the integration constant  $C$  can be determined by the condition  $d\rho/dx = 0$  when  $\rho = \rho_l$  or  $\rho_v$ . Therefore, we have

$$C = \Theta(\rho_l) - \frac{p_{\text{EOS}}(\rho_l)}{\rho_l} = \Theta(\rho_v) - \frac{p_{\text{EOS}}(\rho_v)}{\rho_v}. \quad (11)$$

The right-hand side of Eq. (10) is a nonnegative function of the fluid density  $\rho$ . To simplify the notation, we define

$$\Phi(\rho) \equiv \sqrt{p_{\text{sat}} - \rho\Theta + \rho C}, \quad (12)$$

and then rewrite Eq. (10) as

$$\sqrt{\frac{\kappa}{2}} \left| \frac{d\rho}{dx} \right| = \Phi. \quad (13)$$

Since  $d\rho/dx = 0$  when  $\rho = \rho_l$  and  $\rho_v$ , it can be easily obtained from Eq. (10) that

$$\int_{\rho_v}^{\rho_l} (p_{\text{sat}} - p_{\text{EOS}}) dv = 0, \quad (14)$$

which is known as the Maxwell construction (the equal-area construction in the  $p$ - $v$  plane) in thermodynamic theory. The saturated liquid and vapor densities  $\rho_l$  and  $\rho_v$ , as well as the saturation pressure  $p_{\text{sat}}$ , can be uniquely determined from Eq. (14). Then, the function defined in Eq. (12) can be immediately obtained. Some multiphase EOSs commonly employed in the LB method and their indefinite integrals are summarized in the Appendix.

With the function  $\Phi(\rho)$ , the equilibrium condition given by Eq. (3b) can be rewritten as

$$\Phi - \frac{1}{\sqrt{2\kappa}} \left| \frac{\partial(\rho f_s)}{\partial \rho} \right| = 0 \quad \text{on } \partial\Omega, \quad (15)$$

from which the fluid density  $\rho$  on the solid surface  $\partial\Omega$  can be uniquely determined [27]. In the following, the  $\rho$  on  $\partial\Omega$  is denoted by  $\rho_{sl}$  and  $\rho_{sv}$  when the solid surface is immersed in the bulk liquid and vapor phases, respectively. As shown by Huang *et al.* [27], the contact angle  $\theta$  can be analytically calculated by

$$\cos\theta = \frac{\sigma_{sv} - \sigma_{sl}}{\sigma_{lv}} = \frac{\frac{1}{\sqrt{2\kappa}} [\rho_{sv} f_s(\rho_{sv}) - \rho_{sl} f_s(\rho_{sl})] + \int_{\min(\rho_{sv}, \rho_v)}^{\max(\rho_{sv}, \rho_v)} \Phi d\rho - \int_{\min(\rho_{sl}, \rho_l)}^{\max(\rho_{sl}, \rho_l)} \Phi d\rho}{\int_{\rho_v}^{\rho_l} \Phi d\rho}, \quad (16)$$

where  $\sigma_{lv}$ ,  $\sigma_{sl}$ , and  $\sigma_{sv}$  denote the liquid-vapor, solid-liquid, and solid-vapor surface tensions, respectively. It can be seen

from Eqs. (15) and (16) that the contact angle  $\theta$  is unambiguously determined by the surface free-energy density  $\rho f_s$ ,

or more precisely its derivative  $\partial(\rho f_s)/\partial\rho$  since  $\rho_{sv}f_s(\rho_{sv}) - \rho_{sl}f_s(\rho_{sl})$  in Eq. (16) can be reformulated to the integral  $-\int_{\rho_{sv}}^{\rho_{sl}} [\partial(\rho f_s)/\partial\rho]d\rho$ .

### B. Surface free-energy density

The simplest surface free-energy density is the linear one proposed by Cahn [25]

$$\rho f_s = -\gamma\rho, \quad (17a)$$

$$\frac{\partial(\rho f_s)}{\partial\rho} = -\gamma, \quad (17b)$$

where the parameter  $\gamma$  determines the contact angle. This linear  $\rho f_s$  has been widely adopted in the free-energy LB model for multiphase flows [23,24,26,32]. It is originally proposed for critical point wetting and could induce large deviations between  $\rho_{sl}$  and  $\rho_l$  and between  $\rho_{sv}$  and  $\rho_v$  far from the critical point. To remedy this defect, a hyperbolic tangent surface free-energy density is recently proposed by Huang *et al.* [27]

$$\rho f_s = -\frac{\gamma(\rho_l - \rho_v)}{2\zeta} \tanh\left(\zeta \frac{2\rho - \rho_l - \rho_v}{\rho_l - \rho_v}\right), \quad (18a)$$

$$\frac{\partial(\rho f_s)}{\partial\rho} = -\gamma \operatorname{sech}^2\left(\zeta \frac{2\rho - \rho_l - \rho_v}{\rho_l - \rho_v}\right), \quad (18b)$$

where the parameter  $\zeta$  is used to reduce the deviations between  $\rho_{sl}$  and  $\rho_l$  and between  $\rho_{sv}$  and  $\rho_v$ , and the parameter  $\gamma$  is used to adjust the contact angle. This hyperbolic tangent  $\rho f_s$  has been successfully applied to simulate thermodynamic wetting with liquid-vapor phase transition via the multiphase LB model with self-tuning EOS [27]. In addition, the cubic surface free-energy density [ $\psi_b = -\gamma(\phi^2/2 - \phi^3/3)$ ] has been widely adopted in the phase-field description of the incompressible multiphase flows [33–38], where the densities are assumed to be constant and the temperature is treated as a passive scalar. The details of the multiphase EOS (i.e., the thermophysical properties implied by the multiphase EOS) are not important for the incompressible multiphase flows and thus the double-well bulk free-energy density [ $\psi_b = \beta\phi^2(1 - \phi)^2$ ] is employed to describe the incompressible multiphase fluids. Here,  $\phi$  is the order parameter with  $\phi = 0$  representing one phase and  $\phi = 1$  the other, the free-energy densities  $\psi_s$  and  $\psi_b$  correspond to the present  $\rho f_s$  and  $\rho f_b$ , respectively, and the parameters  $\gamma$  and  $\beta$  are used to adjust the contact angle and surface tension, respectively. Since we focus on the multiphase flows where a realistic multiphase EOS should be specified, this cubic surface free-energy density in the phase-field description of the incompressible multiphase flows will not be further discussed here.

From the above analysis, we can see that the existing surface free-energy densities are proposed without considering any details of the multiphase EOS. However, the surface wettability depends on not only the physicochemical properties of the solid surface but also the thermodynamical properties of the liquid-vapor fluids, implying that the dependence of the contact angle  $\theta$  versus the parameter  $\gamma$  in the aforementioned  $\rho f_s$  [see Eqs. (17) and (18)] is EOS-dependent and also temperature-dependent. Moreover, for the linear and hyperbolic tangent  $\rho f_s$ , the fluid density  $\rho$  on the solid surface

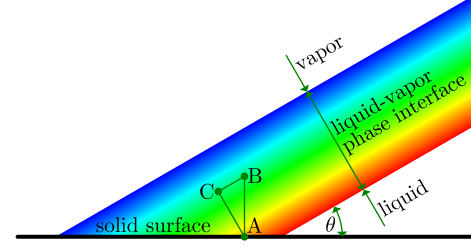


FIG. 1. Enlarged illustration of the three-phase contact point, where point A is on the solid surface,  $\nabla_{\perp\text{wall}}\rho$  and  $\nabla_{\perp\text{interface}}\rho$  on point A are geometrically defined along the line segments BA and CA, respectively, the line segment BC is locally parallel to the liquid-vapor phase interface, and the length ratio of CA to BA is  $\cos\theta$ . Note that when  $\theta > 90^\circ$ ,  $\nabla_{\perp\text{interface}}\rho$  is defined along AC and the length ratio of AC to BA is  $-\cos\theta$ . Moreover, the three-phase contact point is not a geometric point since the liquid-vapor phase interface is diffusive.

$\partial\Omega$  cannot be algebraically determined [see Eq. (15)] and the analytical expression for the contact angle is also very complicated [see Eq. (16)]. Since the function  $\Phi(\rho)$  defined in Eq. (12) can be immediately obtained after the Maxwell construction, we propose a novel EOS-dependent surface free-energy density as follows:

$$\frac{\partial(\rho f_s)}{\partial\rho} = -\gamma\sqrt{2\kappa}\Phi, \quad (19)$$

where the parameter  $\gamma$  determines the contact angle. Before proceeding further, some discussion on the function  $\Phi(\rho)$  is useful. It can be concluded from Eq. (13) that  $\Phi(\rho_l) = \Phi(\rho_v) = 0$  (as  $d\rho/dx = 0$  in the bulk liquid and vapor phases) and  $\Phi(\rho) > 0$  when  $\rho \neq \rho_{l,v}$  (as  $|d\rho/dx| > 0$  in the inhomogeneous regions). With the present EOS-dependent  $\partial(\rho f_s)/\partial\rho$ , the equilibrium condition given in Eq. (15) can be further simplified as

$$\Phi - |\gamma|\Phi = 0 \quad \text{on } \partial\Omega, \quad (20)$$

which immediately leads to

$$\rho_{sl} = \rho_l, \quad \rho_{sv} = \rho_v. \quad (21)$$

Then, the analytical expression for the contact angle, Eq. (16), can be simplified as

$$\cos\theta = \gamma, \quad (22)$$

where the algebraic manipulation  $\rho_{sv}f_s(\rho_{sv}) - \rho_{sl}f_s(\rho_{sl}) = -\int_{\rho_{sv}}^{\rho_{sl}} [\partial(\rho f_s)/\partial\rho]d\rho = \gamma\sqrt{2\kappa} \int_{\rho_v}^{\rho_l} \Phi d\rho$  is used. Equations (21) and (22) are derived from the knowledge of  $\partial(\rho f_s)/\partial\rho$  given by Eq. (19), implying that the exact expression for  $\rho f_s$  is not required in real applications. The physical implication of this point is thermodynamics deals with the change of thermodynamic energy rather than its absolute value. In addition, with the present EOS-dependent surface free-energy density, the analytical expression for the contact angle is very simple, and the equilibrium condition on the solid surface leads to the geometric formulation of the contact angle (see Fig. 1).

It is noteworthy that the contact angle  $\theta$  in Eqs. (16) and (22) is the static contact angle calculated via Young's

equation, where the liquid-vapor, solid-liquid, and solid-vapor surface tensions are theoretically determined for the flat liquid-vapor phase interface and solid surfaces. In thermodynamic theory, the liquid-vapor surface tension, as well as the solid-liquid and solid-vapor surface tensions, is curvature-dependent [7,39–42], which cannot be neglected when the interface thickness is comparable to the interface radius (such as the nanodroplet and nanobubble [43]). However, when the interface thickness is much smaller than the interface radius (such as for the macroscale, or even mesoscale, situation), the dependence of the surface tension with the interface curvature can be safely neglected, and then Eqs. (16) and (22) are applicable to the two- and three-dimensional systems with curved liquid-vapor phase interface and solid surface. With the present EOS-dependent  $\partial(\rho f_s)/\partial\rho$ , the equilibrium condition given by Eq. (3b) can be rewritten as

$$\nabla_{\perp\text{wall}} \rho - \gamma \sqrt{\frac{2}{\kappa}} \Phi = 0 \quad \text{on } \partial\Omega, \quad (23)$$

where  $\nabla_{\perp\text{wall}} \rho$  is a short notation of  $\nabla \rho \cdot \hat{\mathbf{n}}$ , on  $\partial\Omega$  and means the density gradient on the solid surface along its outward normal direction. Assuming that the structure of the liquid-vapor phase interface (i.e., the density profile across the liquid-vapor phase interface) is irrelevant to the geometric configuration, and then with the help of Eqs. (13) and (22), Eq. (23) can be reformulated to

$$\nabla_{\perp\text{wall}} \rho = \cos \theta \left. \frac{d\rho}{dx} \right|_{1D} \approx \cos \theta \nabla_{\perp\text{interface}} \rho \quad \text{on } \partial\Omega, \quad (24)$$

where  $\nabla_{\perp\text{interface}} \rho$  denotes the density gradient along the normal direction of the liquid-vapor phase interface. Here, the normal direction of the liquid-vapor phase interface points from the vapor to liquid phases, implying that  $\nabla_{\perp\text{interface}} \rho \geq 0$ . Figure 1 shows an enlarged illustration of the three-phase contact point, together with the geometric definitions of  $\nabla_{\perp\text{wall}} \rho$  and  $\nabla_{\perp\text{interface}} \rho$  on  $\partial\Omega$ . It can be seen from Fig. 1 that the equilibrium condition given by Eq. (24), which is derived from thermodynamic theory with the present EOS-dependent surface free-energy density, can be interpreted as the geometric formulation of the contact angle [44].

### III. NUMERICAL METHOD

The present EOS-dependent surface free-energy density is proposed from the thermodynamic analysis of surface wettability, and thus it can be applied to any thermodynamically consistent methods/models for multiphase flows. In this work, to numerically validate the EOS-dependent surface free-energy density, the multiphase LB model with self-tuning EOS is employed because the model is based on the underlying microscopic molecular interaction rather than the traditional interface capturing/tracking technique and it is consistent with thermodynamic theory in a strict sense. In this multiphase LB model, the terminology “self-tuning EOS” means that the EOS intrinsically recovered by the LB equation (i.e., by its collision operator without the force term) can be tuned itself via a built-in variable. This self-tuning EOS can be physically interpreted as the incorporation of

the short-range repulsive molecular interaction considering the short-range repulsive molecular interaction can be well modeled by Enskog theory for dense gases. When the pairwise interaction force is introduced into the LB equation to mimic the long-range attractive molecular interaction, a corresponding attractive term is then introduced into the recovered self-tuning EOS to constitute a multiphase EOS [see Eq. (28)]. Therefore, the multiphase LB model with self-tuning EOS is consistent with the kinetic model for multiphase fluids that combines Enskog theory for dense gases and mean-field theory for long-range molecular interaction [17], and the terminology “self-tuning EOS” should not be confused with the arbitrary specification of a realistic multiphase EOS [27]. For the sake of completeness, the multiphase LB model with self-tuning EOS and the corresponding wetting condition treatment are briefly introduced in this section.

#### A. LB model with self-tuning EOS

The multiphase LB model with self-tuning EOS is based on the standard lattice (i.e., the D2Q9 and D3Q27 lattices for the two- and three-dimensional situations, respectively) and the multiple-relaxation-time (MRT) collision operator [16,45]. The MRT LB equation for the density distribution function  $f_i$  is given as

$$f_i(\mathbf{x} + \mathbf{e}_i \delta_t, t + \delta_t) = \bar{f}_i(\mathbf{x}, t), \quad (25a)$$

$$\begin{aligned} \bar{\mathbf{m}} &= \mathbf{m} + \delta_t \mathbf{F}_m - \mathbf{S} \left( \mathbf{m} - \mathbf{m}^{\text{eq}} + \frac{\delta_t}{2} \mathbf{F}_m \right) \\ &+ \mathbf{S} \mathbf{Q}_m - \mathbf{R} \left( \mathbf{I} - \frac{\mathbf{S}}{2} \right) \left( \mathbf{m} - \mathbf{m}^{\text{eq}} + \frac{\delta_t}{2} \mathbf{F}_m \right) \\ &- \delta_x \mathbf{T} \nabla \rho - \delta_x \mathbf{X} \nabla \eta, \end{aligned} \quad (25b)$$

where Eqs. (25a) and (25b) denote the *linear* streaming process in velocity space and the *local* collision process in moment space (locally computed at position  $\mathbf{x}$  and time  $t$ ), respectively, and the overbar denotes the post-collision state. The transformations between velocity and moment spaces are performed via  $\mathbf{m} = \mathbf{M}(f_i)^T$  and  $(f_i)^T = \mathbf{M}^{-1} \mathbf{m}$  with  $(f_i)^T$  a short notation of the lattice vector  $(f_0, f_1, \dots, f_{N-1})^T$ ,  $\mathbf{m}$  the moment of  $(f_i)^T$ , and  $\mathbf{M}$  the orthogonal transformation matrix. In the *local* collision process, the first three terms  $\mathbf{m} + \delta_t \mathbf{F}_m - \mathbf{S}(\mathbf{m} - \mathbf{m}^{\text{eq}} + \frac{\delta_t}{2} \mathbf{F}_m)$  constitute the classical MRT collision operator, the term  $+\mathbf{S} \mathbf{Q}_m$  is a consistent scheme for the  $\varepsilon^3$ -order term for multiphase flows [46,47], and the last three terms  $-\mathbf{R}(\mathbf{I} - \frac{\mathbf{S}}{2})(\mathbf{m} - \mathbf{m}^{\text{eq}} + \frac{\delta_t}{2} \mathbf{F}_m) - \delta_x \mathbf{T} \nabla \rho - \delta_x \mathbf{X} \nabla \eta$  are aimed to eliminate the additional cubic terms of velocity in recovering the Newtonian viscous stress [27,48], which should be seriously considered rather than directly ignored for multiphase flows [49]. In the LB equation,  $\mathbf{e}_i$  is the discrete velocity,  $\delta_x$  is the lattice spacing,  $\delta_t$  is the time step,  $\mathbf{S}$  is the collision matrix,  $\mathbf{m}^{\text{eq}}$  is the equilibrium moment,  $\mathbf{F}_m$  is the discrete force,  $\mathbf{Q}_m$  is the  $\varepsilon^2$ -order source term,  $\mathbf{I}$  is the unit matrix, and  $\mathbf{R}$ ,  $\mathbf{T}$ , and  $\mathbf{X}$  are  $N \times N$ ,  $N \times D$ , and  $N \times D$  matrices, respectively, with  $N$  the number of discrete velocities and  $D$  the dimension of space. Since this work focuses on the surface free-energy density for wettability in thermodynamic theory, the technical details of the above LB equation will not be

covered here, and the reader is referred to our previous works [16,27,45].

In the multiphase LB model with self-tuning EOS, the short-range molecular interaction is inherently incorporated by the MRT collision operator, and the long-range molecular interaction is mimicked by the pairwise interaction force

$$\mathbf{F}_{\text{int}}(\mathbf{x}) = G^2 \rho(\mathbf{x}) \sum_{i=1}^{N-1} \omega(|\mathbf{e}_i \delta_t|^2) \rho(\mathbf{x} + \mathbf{e}_i \delta_t) \mathbf{e}_i \delta_t, \quad (26)$$

where  $G$  is the interaction strength,  $\omega(|\mathbf{e}_i \delta_t|^2)$  is the distance-dependent weight satisfying  $\sum_{i=1}^{N-1} \omega(|\mathbf{e}_i \delta_t|^2) \mathbf{e}_i \mathbf{e}_i = c^2 \mathbf{I}$  and  $\sum_{i=1}^{N-1} \omega(|\mathbf{e}_i \delta_t|^2) \mathbf{e}_i \mathbf{e}_i \mathbf{e}_i = c^4 \mathbf{II}/3$  to maximize the isotropy degree of  $\mathbf{F}_{\text{int}}$ . Here,  $c = \delta_x / \delta_t$  is the lattice speed,  $\mathbf{I} = \delta_{\alpha\beta}$  is the unit tensor, and  $\mathbf{II} = \delta_{\alpha\beta} \delta_{\gamma\delta} + \delta_{\alpha\gamma} \delta_{\beta\delta} + \delta_{\alpha\delta} \delta_{\beta\gamma}$ . The macroscopic density  $\rho$  and momentum  $\rho \mathbf{u}$  are defined as

$$\rho = \sum_{i=0}^{N-1} f_i, \quad \rho \mathbf{u} = \sum_{i=0}^{N-1} \mathbf{e}_i f_i + \frac{\delta_t}{2} \mathbf{F}, \quad (27)$$

where  $\mathbf{F}$  is the total force that consists of the pairwise interaction force  $\mathbf{F}_{\text{int}}$  and the other external force  $\mathbf{F}_{\text{ext}}$  if it exists in real applications. The multiphase EOS is recovered as

$$p_{\text{EOS}} = p_{\text{LBE}} - \frac{G^2 \delta_x^2}{2} \rho^2 = c_s^2 (\rho + \eta) - \frac{G^2 \delta_x^2}{2} \rho^2, \quad (28)$$

where the first term  $p_{\text{LBE}} = c_s^2 (\rho + \eta)$ , with  $\eta$  the built-in variable in  $\mathbf{m}^{\text{eq}}$  and  $c_s = c / \sqrt{3}$  the lattice sound speed, is the self-tuning EOS implied by the MRT collision operator and the second term  $-G^2 \delta_x^2 \rho^2 / 2$  is introduced by the pairwise interaction force.

In the following numerical validations, the Carnahan-Starling EOS [50] is chosen as an example,

$$p_{\text{EOS}} = K_{\text{EOS}} \left[ \rho RT \frac{1 + b\rho/4 + (b\rho/4)^2 - (b\rho/4)^3}{(1 - b\rho/4)^3} - a\rho^2 \right], \quad (29a)$$

of which the indefinite integral can be calculated as

$$\begin{aligned} \Theta &= \int p_{\text{EOS}} dv \\ &= K_{\text{EOS}} \left[ -RT \frac{3 - b\rho/2}{(1 - b\rho/4)^2} - RT \ln \rho + a\rho \right]. \end{aligned} \quad (29b)$$

Here, the scaling factor  $K_{\text{EOS}}$  is introduced to adjust the liquid-vapor surface tension, and the coefficients  $a$  and  $b$  are related to the critical properties via the critical conditions  $(\partial p_{\text{EOS}} / \partial \rho)_T = 0$  and  $(\partial^2 p_{\text{EOS}} / \partial \rho^2)_T = 0$  as follows:

$$\begin{aligned} a &= 1.3828652346415909 \frac{RT_{\text{cr}}}{\rho_{\text{cr}}}, \\ b &= 0.5217755367698158 \frac{1}{\rho_{\text{cr}}}, \end{aligned} \quad (30)$$

where  $T_{\text{cr}}$  and  $\rho_{\text{cr}}$  are the critical temperature and density, respectively. Note that the coefficient  $b$  in  $p_{\text{EOS}}$  here should not be confused with the  $b$  in the collision matrix  $\mathbf{S}$  of the LB equation (see Eq. (6) in Ref. [16]). The critical pressure  $p_{\text{cr}}$  can be directly calculated via the multiphase EOS with  $T_{\text{cr}}$  and  $\rho_{\text{cr}}$ , and the reduced temperature is defined as  $T_r = T / T_{\text{cr}}$ .

When the Carnahan-Starling EOS is specified in the multiphase LB model with self-tuning EOS, the interaction strength is set to [16]

$$G = K_{\text{INT}} \sqrt{2K_{\text{EOS}} \frac{a}{\delta_x^2}}, \quad (31a)$$

and the lattice sound speed is chosen as

$$c_s = K_{\text{INT}} \sqrt{\left( \frac{\partial p_{\text{EOS}}}{\partial \rho} \right)_T + 2K_{\text{EOS}} a \rho} \Bigg|_{\rho=\rho_l}, \quad (31b)$$

where the scaling factor  $K_{\text{INT}}$  is introduced to adjust the liquid-vapor interface thickness. Once a realistic multiphase EOS is specified in real applications, the built-in variable  $\eta$  in  $\mathbf{m}^{\text{eq}}$  is then inversely calculated by  $\eta = p_{\text{EOS}} / c_s^2 + G^2 \delta_x^2 \rho^2 / (2c_s^2) - \rho$  [see Eq. (28)]. The liquid-vapor surface tension and interface thickness satisfy  $\sigma_{lv} \propto K_{\text{EOS}} K_{\text{INT}}$  and  $W_{lv} \propto K_{\text{INT}}$ , respectively, where the proportionality constants can be analytically determined in advance [16,45]. Considering the liquid-vapor phase interface is diffusive (see Fig. 1 as an illustration), the interface thickness is defined from  $\rho = 0.95\rho_v + 0.05\rho_l$  to  $0.05\rho_v + 0.95\rho_l$  and the interface position is defined at  $\rho = 0.5\rho_v + 0.5\rho_l$  throughout this work. Before proceeding further, it is worth pointing out that there is no need to explicitly introduce the scaling factors  $K_{\text{EOS}}$  and  $K_{\text{INT}}$  into the present  $\partial(\rho f_s) / \partial \rho$  given by Eq. (19) to ensure that the contact angle  $\theta$ , the surface tension  $\sigma_{lv}$ , and the interface thickness  $W_{lv}$  can be independently adjusted in real applications because  $K_{\text{EOS}}$  and  $K_{\text{INT}}$  are implicitly included in  $\partial(\rho f_s) / \partial \rho$  via  $\kappa$  and  $\Phi$ .

## B. Wetting condition treatment

The wettability of the liquid-vapor fluids on a solid surface can be implemented by enforcing the equilibrium condition there [see Eq. (23) for the present EOS-dependent surface free-energy density or Eq. (3b) for the general case], and the wetting condition treatment proposed by Huang *et al.* [27] is adopted here. Note that the two-dimensional situation is considered by Huang *et al.* [27], and we extend it to the three-dimensional situation in this work. In Huang *et al.*'s wetting condition treatment, the solid surface is represented by a series of wall nodes, and the LB simulation is performed on the fluid and wall nodes but not the solid nodes. After the streaming process [i.e., Eq. (25a)], some of the distribution functions on the wall node are unknown due to the absence of the adjacent fluid/wall nodes, as shown by Figs. 2 and 3 for the two- and three-dimensional situations, respectively.

The fluid density on the wall node is first determined via an auxiliary bounce-back process, i.e., the post-collision density distribution function hitting the solid surface reverses its direction as follows [51]:

$$f_{i,\text{unknown}}(\mathbf{x}_{\text{wall}}, t + \delta_t) = \bar{f}_i(\mathbf{x}_{\text{wall}}, t), \quad (32)$$

where  $\bar{i}$  denotes the reverse direction of  $i$ , and the subscript ‘‘unknown’’ means that the density distribution function in direction  $\bar{i}$  is unknown after the streaming process. The mass conservation on the wall node can be strictly satisfied by the auxiliary bounce-back process. With this auxiliary bounce-back process, all the unknown density distribution functions

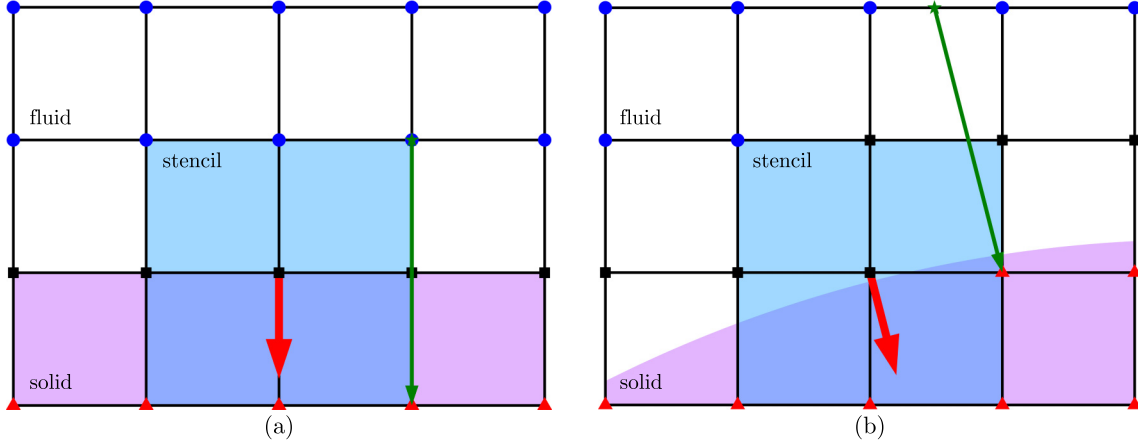


FIG. 2. Illustration of the wetting condition treatment for (a) flat surface and (b) curved surface for the two-dimensional situation. The circular, square, and triangular points denote the fluid, wall, and solid nodes, respectively, and the star denotes a virtual fluid point. The thick arrow is the outward unit normal vector on the wall node, and the thin arrow indicates the density on one solid node is calculated based on the density on its corresponding virtual fluid point.

on the wall node are temporarily obtained and then the density  $\rho(\mathbf{x}_{\text{wall}}, t + \delta_t)$  can be calculated via the definition  $\rho = \sum_{i=0}^{N-1} f_i$ .

The key point of the wetting condition treatment is to determine the pairwise interaction force on the wall node, which can be defined via Eq. (26) as normal. In the interaction stencil as illustrated in Figs. 2 and 3, the densities on all the fluid and wall nodes are already known, and the remaining task is to determine the densities on the solid nodes, which can be done under the equilibrium condition from thermodynamic theory [i.e., Eq. (23)]. For this purpose, a virtual fluid point is set along the inward normal direction [27]

$$\mathbf{x}_{\text{vf}} = \mathbf{x}_{\text{solid}} - \frac{2\delta_x}{\max(|\hat{n}_{s,\alpha}|)} \hat{\mathbf{n}}_s, \quad (33)$$

where  $\max(|\hat{n}_{s,\alpha}|)$  denotes the maximum magnitude of the elements of the outward unit normal vector  $\hat{\mathbf{n}}_s$ . For the flat surface, the virtual fluid point overlaps with a fluid node, implying that  $\rho(\mathbf{x}_{\text{vf}}, t + \delta_t)$  is immediately known. For the

curved surface, the virtual fluid point lies on a grid line and face for the two- and three-dimensional situations, respectively, as shown in Figs. 2 and 3, and then  $\rho(\mathbf{x}_{\text{vf}}, t + \delta_t)$  is calculated using the linear and bilinear interpolations, respectively. Once  $\rho(\mathbf{x}_{\text{vf}}, t + \delta_t)$  is obtained, the density on the solid node is evaluated under Eq. (23),

$$\rho(\mathbf{x}_{\text{solid}}, t + \delta_t) = \rho(\mathbf{x}_{\text{vf}}, t + \delta_t) + \frac{2\delta_x}{\max(|\hat{n}_{s,\alpha}|)} \gamma \sqrt{\frac{2}{\kappa}} \Phi. \quad (34)$$

Note that there could be more than one solid node in the interaction stencil, and the density on each solid node should be individually evaluated via Eqs. (33) and (34) for the sake of accuracy. Meanwhile, the function  $\Phi(\rho)$  on the right-hand side of Eq. (34) is related to the fluid density on the solid surface, which is approximated by the following average one in real applications [27]:

$$\rho_{\text{ave}} = \frac{\sum_{i=0}^{N-1} s(\mathbf{x}_{\text{wall}} + \mathbf{e}_i \delta_t) \rho(\mathbf{x}_{\text{wall}} + \mathbf{e}_i \delta_t, t + \delta_t)}{\sum_{i=0}^{N-1} s(\mathbf{x}_{\text{wall}} + \mathbf{e}_i \delta_t)}, \quad (35)$$

where  $s(\mathbf{x}_{\text{wall}} + \mathbf{e}_i \delta_t)$  is a switch function that equals 1 for the fluid and wall nodes while 0 for the solid node. After the densities on all the solid nodes in the interaction stencil are obtained, the pairwise interaction force  $\mathbf{F}_{\text{int}}(\mathbf{x}_{\text{wall}}, t + \delta_t)$  can then be calculated via the definition  $\mathbf{F}_{\text{int}}(\mathbf{x}) = G^2 \rho(\mathbf{x}) \sum_{i=1}^{N-1} \omega(|\mathbf{e}_i \delta_t|^2) \rho(\mathbf{x} + \mathbf{e}_i \delta_t) \mathbf{e}_i \delta_t$ .

At last, all the density distribution functions on the wall node are reconstructed by the improved nonequilibrium-extrapolation scheme to ensure that the momentum definition  $\rho \mathbf{u} = \sum_{i=0}^{N-1} \mathbf{e}_i f_i + \delta_t \mathbf{F}/2$  precisely holds on the wall node [51]. For this purpose, the moment of the density distribution function is decomposed into the equilibrium, force, and nonequilibrium parts,

$$\mathbf{m} = \mathbf{m}^{\text{eq}} - \frac{\delta_t}{2} \mathbf{F}_m + \mathbf{m}^{\text{neq}}, \quad (36a)$$

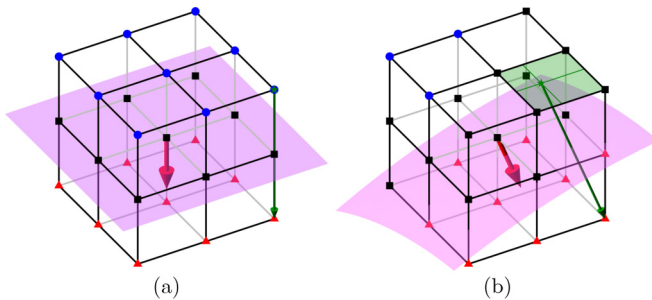


FIG. 3. Illustration of the wetting condition treatment for (a) flat surface and (b) curved surface for the three-dimensional situation. The circular, square, and triangular points denote the fluid, wall, and solid nodes, respectively, and the star denotes a virtual fluid point. The thick arrow is the outward unit normal vector on the wall node, and the thin arrow indicates the density on one solid node is calculated based on the density on its corresponding virtual fluid point.

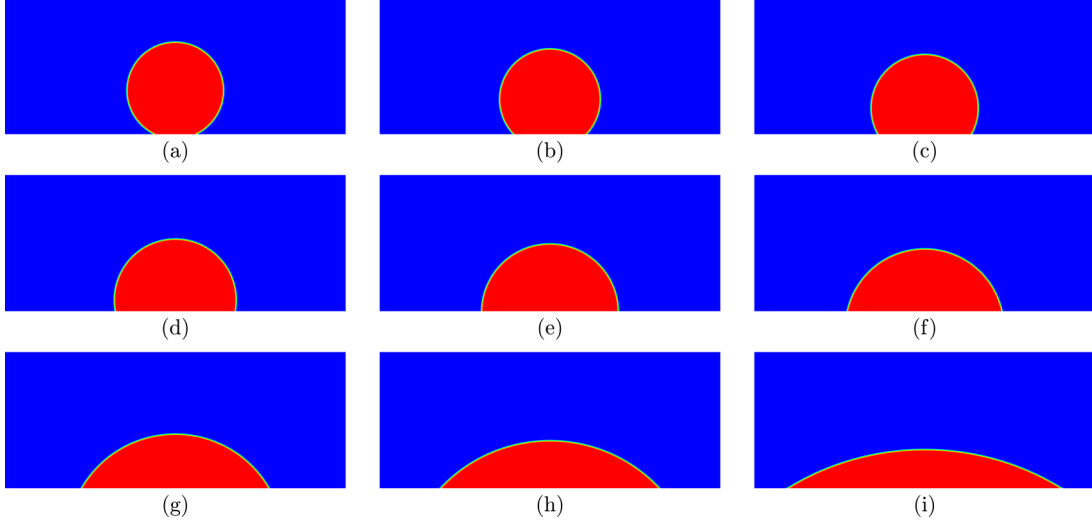


FIG. 4. Density contours of the static droplet on flat surface obtained by the two-dimensional LB simulations with (a)  $\gamma = -0.9$ , (b)  $\gamma = -0.7$ , (c)  $\gamma = -0.5$ , (d)  $\gamma = -0.2$ , (e)  $\gamma = 0$ , (f)  $\gamma = 0.2$ , (g)  $\gamma = 0.5$ , (h)  $\gamma = 0.7$ , and (i)  $\gamma = 0.9$ . The reduced temperature is  $T_r = 0.7$ , and the liquid-vapor surface tension and interface thickness are  $\sigma_{lv} = 0.01$  and  $W_{lv} = 10$ , respectively.

and an improved extrapolation term is introduced,

$$\tilde{\mathbf{m}}^{\text{neq}} = \left( \mathbf{I} - \frac{\mathbf{S}}{2} \right) \mathbf{m}^{\text{neq}}. \quad (36b)$$

On the wall node, the equilibrium part  $\mathbf{m}^{\text{eq}}(\mathbf{x}_{\text{wall}}, t + \delta_t)$  and the force part  $-\delta_t \mathbf{F}_m(\mathbf{x}_{\text{wall}}, t + \delta_t)/2$  can be directly calculated as  $\rho(\mathbf{x}_{\text{wall}}, t + \delta_t)$  and  $\mathbf{F}_{\text{int}}(\mathbf{x}_{\text{wall}}, t + \delta_t)$  are already obtained, while the nonequilibrium part  $\mathbf{m}^{\text{neq}}(\mathbf{x}_{\text{wall}}, t + \delta_t)$  is determined by extrapolating  $\tilde{\mathbf{m}}$  from the nearest fluid node as follows:

$$\tilde{\mathbf{m}}^{\text{neq}}(\mathbf{x}_{\text{wall}}, t + \delta_t) = \tilde{\mathbf{m}}^{\text{neq}}(\mathbf{x}_{\text{fluid}}, t + \delta_t). \quad (37)$$

Once  $\tilde{\mathbf{m}}^{\text{neq}}(\mathbf{x}_{\text{wall}}, t + \delta_t)$  is obtained,  $\mathbf{m}^{\text{neq}}(\mathbf{x}_{\text{wall}}, t + \delta_t)$  can be inversely determined via Eq. (36b), and  $\mathbf{m}(\mathbf{x}_{\text{wall}}, t + \delta_t)$  can be constructed via Eq. (36a). Therefore, all the density distribution functions  $f_i(\mathbf{x}_{\text{wall}}, t + \delta_t)$  can be updated via the space transformation  $(f_i)^T = \mathbf{M}^{-1} \mathbf{m}$ . Note that Eq. (37) is the first-order extrapolation, and in real applications, the second-order extrapolation can also be adopted for the sake of accuracy [51]. Through the aforementioned procedures, both the wetting and nonslip conditions on the solid surface are achieved.

#### IV. NUMERICAL VALIDATIONS

In this section, the two- and three-dimensional LB simulations of static droplets on flat and curved surfaces are carried out to validate the present EOS-dependent surface free-energy density for wettability and the derived analytical expression for the contact angle. Then, the three-dimensional LB simulation of a moving droplet on an inclined wall, which is vertically and sinusoidally oscillated, is carried out. In the LB simulations, the lattice spacing is fixed at  $\delta_x = 1$ , the lattice sound speed  $c_s$  is determined by Eq. (31b), and then the lattice speed and time step are calculated by  $c = \sqrt{3}c_s$  and  $\delta_t = \delta_x/c$ , respectively. The other basic parameters of the two- and three-dimensional LB models are chosen following Refs. [27] and [45], respectively. The coefficients in the Carnahan-Starling EOS are set to  $a = 1$ ,  $b = 4$ , and  $R = 1$ .

The reduced temperature  $T_r$ , the liquid-vapor surface tension  $\sigma_{lv}$ , and the liquid-vapor interface thickness  $W_{lv}$  will be individually stated in practical simulations, by which the scaling factors  $K_{\text{EOS}}$  and  $K_{\text{INT}}$  can be determined.

##### A. Static droplet on flat surface

First, a static droplet on a flat surface is considered. The reduced temperature is set to  $T_r = 0.7$ , and thus the saturated liquid and vapor densities are  $\rho_l = 0.358131$  and  $\rho_v = 0.00929415$ . The liquid-vapor surface tension and interface thickness are fixed at  $\sigma_{lv} = 0.01$  and  $W_{lv} = 10$ , implying that the scaling factors are  $K_{\text{EOS}} = 0.201280$  and  $K_{\text{INT}} = 2.905016$ . For the two- and three-dimensional LB simulations, the computational domains are set to  $2048 \times 512$  and  $320 \times 320 \times 120$ , respectively, and the solid surfaces are put on the  $x$  plane with  $y = 0$  and  $x$ - $y$  plane with  $z = 0$ , respectively. The symmetric boundary condition is applied on the opposite plane of the solid surface, and the periodic boundary conditions are applied in the other directions. The density and velocity fields are initialized as

$$\rho(\mathbf{x}, 0) = \frac{\rho_l + \rho_v}{2} - \frac{\rho_l - \rho_v}{2} \tanh \frac{|\mathbf{x} - \mathbf{x}_c| - r_0}{W_{lv}/\ln(19)}, \quad (38a)$$

$$\mathbf{u}(\mathbf{x}, 0) = \mathbf{0}, \quad (38b)$$

where  $\mathbf{x}_c$  is  $(1024, 0)^T$  and  $(160, 160, 0)^T$ , respectively, and  $r_0$  is 256 and 64, respectively, for the two- and three-dimensional LB simulations. The dimensionless relaxation time  $\tau$  is fixed at 1.5 in the simulations.

Figures 4 and 5 show the static droplets in the converged state for the two- and three-dimensional LB simulations, respectively, where the parameter  $\gamma$  in the EOS-dependent surface free-energy density [see Eq. (19)] is set to  $\pm 0.9$ ,  $\pm 0.7$ ,  $\pm 0.5$ ,  $\pm 0.2$ , and 0. As can be seen, the wettability of the liquid-vapor fluids on a flat surface with the analytical contact angle varying from  $\theta = \arccos(-0.9) \approx 154.158^\circ$  to  $\theta = \arccos(0.9) \approx 25.842^\circ$  can be successfully handled by the present multiphase LB model and its wetting condition

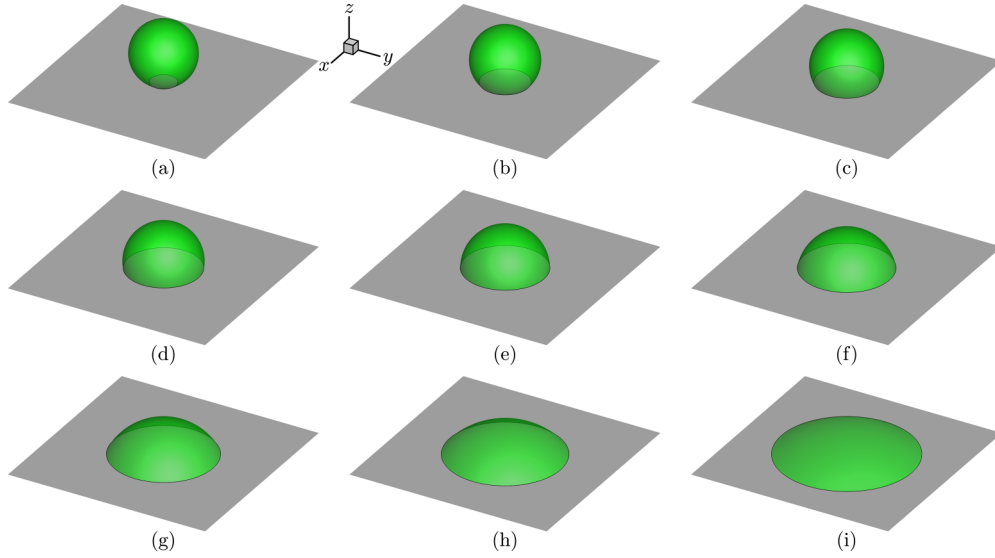


FIG. 5. Interface positions of the static droplet on flat surface obtained by the three-dimensional LB simulations with (a)  $\gamma = -0.9$ , (b)  $\gamma = -0.7$ , (c)  $\gamma = -0.5$ , (d)  $\gamma = -0.2$ , (e)  $\gamma = 0$ , (f)  $\gamma = 0.2$ , (g)  $\gamma = 0.5$ , (h)  $\gamma = 0.7$ , and (i)  $\gamma = 0.9$ . The reduced temperature is  $T_r = 0.7$ , and the liquid-vapor surface tension and interface thickness are  $\sigma_{lv} = 0.01$  and  $W_{lv} = 10$ , respectively.

treatment. Moreover, the numerically achieved contact angle can be effectively adjusted by the parameter  $\gamma$  in the EOS-dependent surface free-energy density. From the density contours in Fig. 4, the interfacial film above the solid surface [20] is indistinguishable as  $\rho_{sl} = \rho_l$  and  $\rho_{sv} = \rho_v$  can be ensured by the present EOS-dependent surface free-energy density [see Eq. (21)].

For quantitative comparison, the contact angle is numerically measured by fitting the liquid-vapor phase interface with a circular/spherical profile. Figure 6 shows the comparison of the contact angles obtained by the two- and three-dimensional LB simulations with the analytical result derived from thermodynamic theory [see Eq. (22)]. It can

be seen from the figure that the contact angles by both the two- and three-dimensional LB simulations correspond well with the analytical result in the range  $-0.9 \leq \gamma \leq 0.9$ . Such a good agreement validates the thermodynamic analysis in Sec. II and the numerical method (including the multiphase LB model with self-tuning EOS and its wetting condition treatment) in Sec. III. In Fig. 6, the variations of the absolute error, defined as  $\delta\theta = \theta_{\text{numerical}} - \theta_{\text{analytical}}$  with  $\theta_{\text{numerical}}$  and  $\theta_{\text{analytical}}$  denoting the numerical and analytical results, with the contact angle is also plotted. As it can be seen, the absolute error falls in the range  $-1^\circ \leq \delta\theta \leq 1^\circ$  when the contact angle  $\theta$  is close to  $90^\circ$  and gradually increases when the contact angle  $\theta$  tends to  $0^\circ$  and  $180^\circ$  (i.e., the parameter  $\gamma$  tends to  $\pm 1$ ). This deviation between the numerical and analytical results shown in Fig. 6 is caused by the numerical error of the wetting condition treatment.

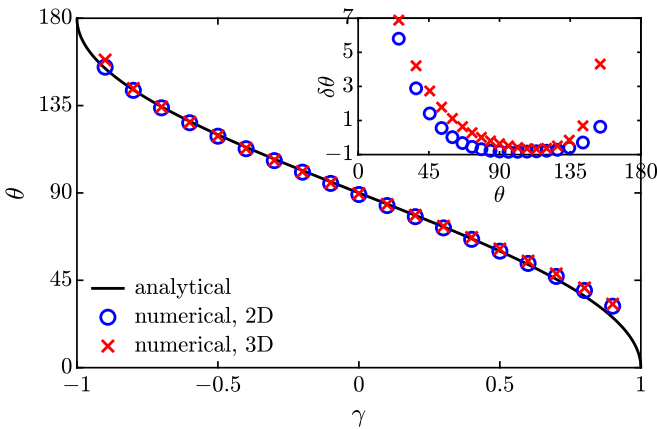


FIG. 6. Comparison of the contact angle obtained by the LB simulation of a static droplet on a flat surface with the analytical result derived from thermodynamic theory, where the variation of the absolute error between the numerical and analytical results with the contact angle is also plotted. The reduced temperature is  $T_r = 0.7$ , and the liquid-vapor surface tension and interface thickness are  $\sigma_{lv} = 0.01$  and  $W_{lv} = 10$ , respectively.

### B. Static droplet on curved surface

To further demonstrate the capability of the present multiphase LB model and its wetting condition treatment, a static droplet on a curved surface is simulated in this section. The reduced temperature is set to  $T_r = 0.8$ , and the saturated liquid and vapor densities are  $\rho_l = 0.307196$  and  $\rho_v = 0.0217232$ , respectively. The liquid-vapor surface tension and interface thickness are chosen as  $\sigma_{lv} = 0.01$  and  $W_{lv} = 10$  unless otherwise stated, implying that  $K_{\text{EOS}} = 0.479820$  and  $K_{\text{INT}} = 2.294922$ . For the two-dimensional LB simulation, the computational domain is  $1024 \times 1024$ , and a solid circle of radius 256 and center  $(512, 384)^T$  is placed in the domain. As for the three-dimensional LB simulation, the computational domain is  $256 \times 256 \times 320$ , and a solid sphere of radius 80 and center  $(128, 128, 112)^T$  is placed in the domain. The solid surface inside the computational domain is handled by the wetting condition treatment in Sec. III B, and the surrounding boundaries of the computational domain are set

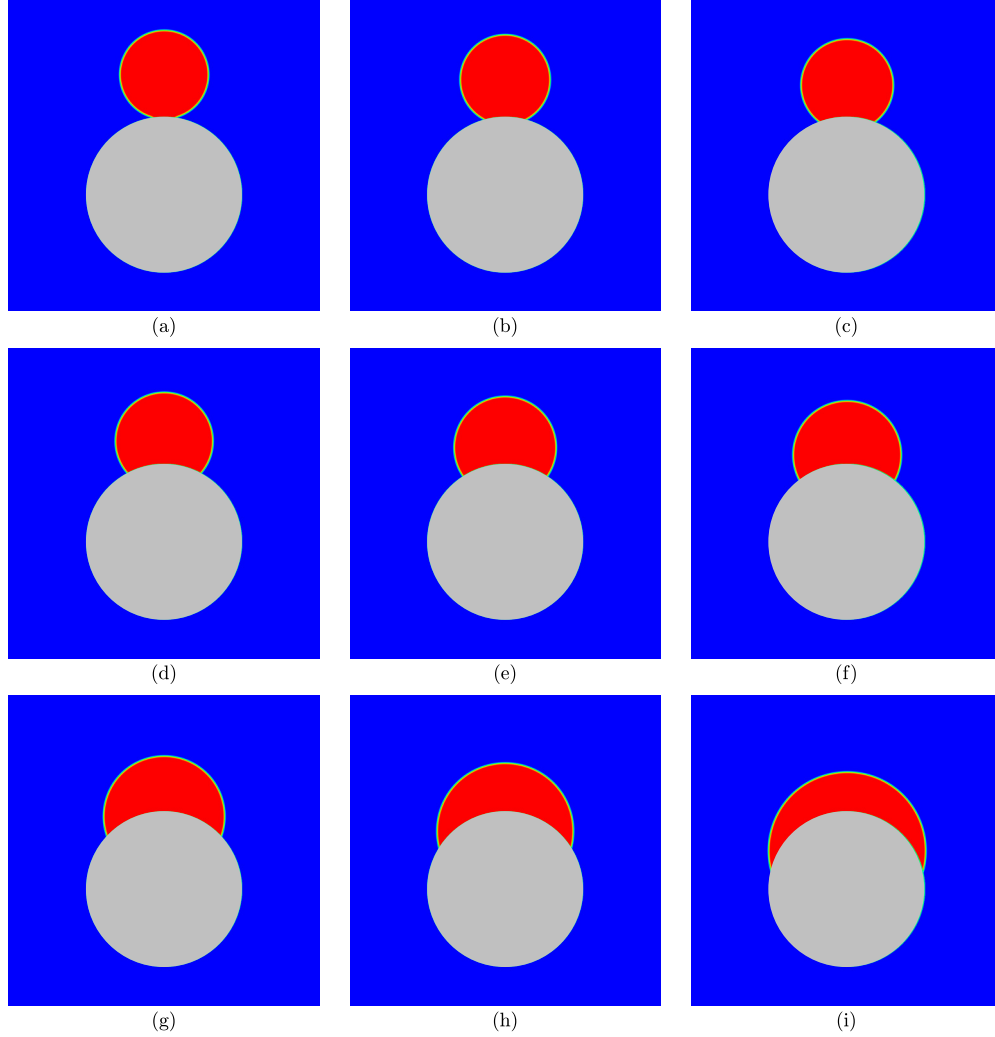


FIG. 7. Density contours of the static droplet on curved surface obtained by the two-dimensional LB simulations with (a)  $\gamma = -0.9$ , (b)  $\gamma = -0.7$ , (c)  $\gamma = -0.5$ , (d)  $\gamma = -0.2$ , (e)  $\gamma = 0$ , (f)  $\gamma = 0.2$ , (g)  $\gamma = 0.5$ , (h)  $\gamma = 0.7$ , and (i)  $\gamma = 0.9$ . The reduced temperature is  $T_r = 0.8$ , and the liquid-vapor surface tension and interface thickness are  $\sigma_{lv} = 0.01$  and  $W_{lv} = 10$ , respectively.

as periodic. Initially, a droplet is deposited on the curved surface as

$$\rho(\mathbf{x}, 0) = \frac{\rho_l + \rho_v}{2} - \frac{\rho_l - \rho_v}{2} \tanh \frac{|\mathbf{x} - \mathbf{x}_c| - r_0}{W_{lv}/\ln(19)}, \quad (39a)$$

$$\mathbf{u}(\mathbf{x}, 0) = \mathbf{0}, \quad (39b)$$

where  $\mathbf{x}_c$  is set to  $(512, 640)^T$  and  $(128, 128, 192)^T$  for the two- and three-dimensional simulations, respectively, and  $r_0$  is set to 192 and 64 for the two- and three-dimensional simulations, respectively. Then, the wetting process of the initial droplet on the curved surface is run to a converged state, where the dimensionless relaxation time  $\tau = 1.5$  in the LB simulations.

Figures 7 and 8 show the final droplets on the circular and spherical solid surfaces for the two- and three-dimensional LB simulations, respectively, where the parameter  $\gamma$  in the EOS-dependent surface free-energy density is set to  $\pm 0.9$ ,  $\pm 0.7$ ,  $\pm 0.5$ ,  $\pm 0.2$ , and 0. The satisfying results shown in Figs. 7 and 8 demonstrate the capability of the present wetting condition

treatment for the two- and three-dimensional curved surfaces. Note that the droplet detaches from the spherical solid surface when the analytical contact angle  $\theta = \arccos(-0.9) \approx 154.158^\circ$  [see Fig. 8(a)], which is caused by the intersection between the diffusive phase interface with the solid surface as illustrated in Fig. 9(a). Since the liquid-vapor phase interface is diffusive rather than sharp and the radii of both the droplet and solid sphere are relatively small, the highest point of the solid surface [i.e., point A in Fig. 9(a)] lies within the diffusive phase interface, and such point of the phase interface could also lie within the unstable region implied by the multiphase EOS (i.e., the region with negative isothermal compressibility bounded by the spinodal curve). Based on the above analysis, this detaching phenomenon could be avoided by decreasing the liquid-vapor interface thickness or increasing the radii of the droplet and solid sphere. Therefore, we repeat the three-dimensional LB simulation with  $\gamma = -0.9$  by decreasing  $W_{lv}$  from 10 to 5 and keeping the other parameters unchanged. The numerical results are shown in Figs. 9(b) and 9(c). As expected, the droplet stays on the spherical solid surface with

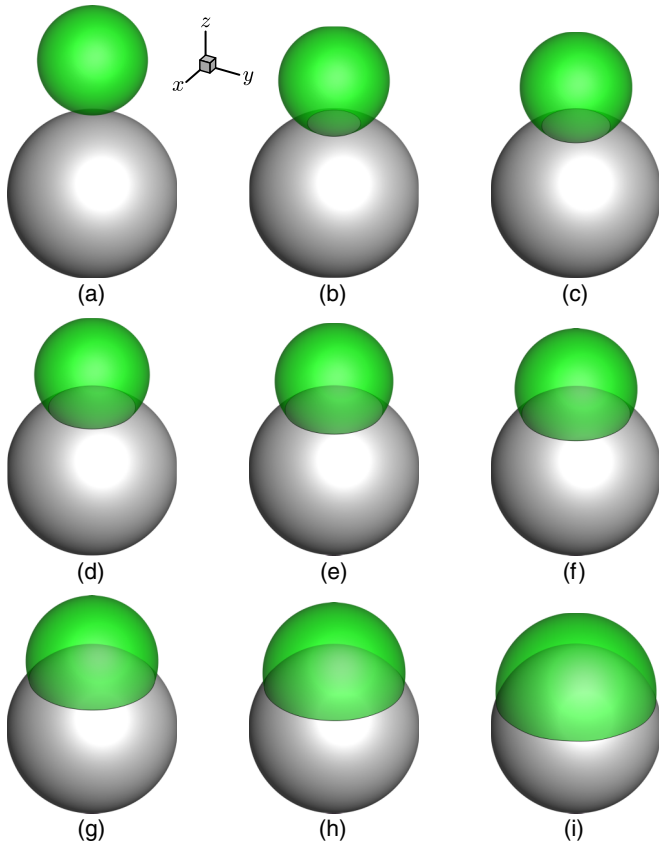


FIG. 8. Interface positions of the static droplet on curved surface obtained by the three-dimensional LB simulations with (a)  $\gamma = -0.9$ , (b)  $\gamma = -0.7$ , (c)  $\gamma = -0.5$ , (d)  $\gamma = -0.2$ , (e)  $\gamma = 0$ , (f)  $\gamma = 0.2$ , (g)  $\gamma = 0.5$ , (h)  $\gamma = 0.7$ , and (i)  $\gamma = 0.9$ . The reduced temperature is  $T_r = 0.8$ , and the liquid-vapor surface tension and interface thickness are  $\sigma_{lv} = 0.01$  and  $W_{lv} = 10$ , respectively.

a very large contact angle, which confirms the above analysis on the detaching phenomenon.

For quantitative comparison, the contact angle is numerically measured by fitting the liquid-vapor phase interface with a circular/spherical profile. The comparison of the numerical results by the two- and three-dimensional LB simulations with the analytical result from thermodynamic theory is shown in Fig. 10. Note that all the numerical results in the figure are simulated with the liquid-vapor interface thickness  $W_{lv} = 10$ , except the three-dimensional one for  $\gamma = -0.9$ , which is simulated with  $W_{lv} = 5$  as mentioned above. As can be seen from Fig. 10, the contact angles by the two- and three-dimensional simulations agree well with the analytical result, which further validates the applicabilities of the EOS-dependent surface free-energy density for wettability and the wetting condition treatment for curved surfaces. Similar to Fig. 6 for the flat surface, a slight deviation between the numerical and analytical results can be observed in Fig. 10 when the parameter  $\gamma$  tends to  $\pm 1$  (the contact angle  $\theta$  tends to  $0^\circ$  and  $180^\circ$ ). Compared with the deviation when  $\theta \rightarrow 0^\circ$ , the deviation when  $\theta \rightarrow 180^\circ$  is relatively large, which could be caused by the aforementioned intersection between the diffusive phase interface with the solid surface (see Fig. 9).

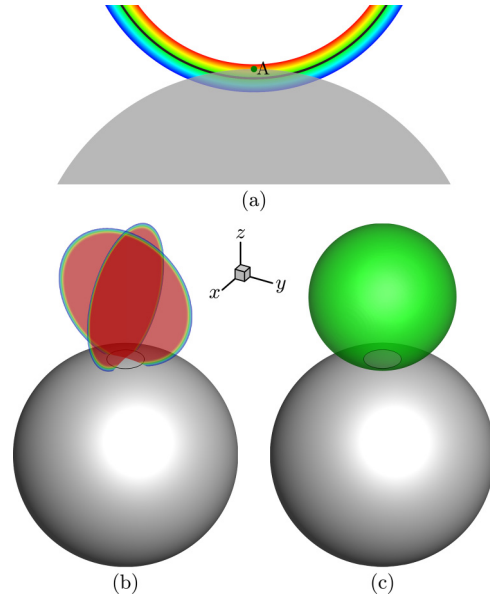


FIG. 9. Static droplet on a curved surface with the analytical contact angle  $\theta = \arccos(-0.9) \approx 154.158^\circ$ . (a) Schematic of the cross-sectional view of the intersection between the diffusive phase interface with the solid surface, where the solid line denotes the interface position defined at  $\rho = 0.5\rho_v + 0.5\rho_l$ . (b) Cross-sectional density contours and (c) interface position of the droplet obtained by the three-dimensional LB simulation with  $\gamma = -0.9$ . The reduced temperature is  $T_r = 0.8$ , and the liquid-vapor surface tension and interface thickness are  $\sigma_{lv} = 0.01$  and  $W_{lv} = 5$ , respectively.

### C. Moving droplet on inclined wall

At last, a moving droplet on an inclined wall, which is vertically and sinusoidally oscillated, is simulated to show the capabilities of the EOS-dependent surface free-energy density, the multiphase LB model with self-tuning EOS, and the wetting condition treatment. In the three-dimensional

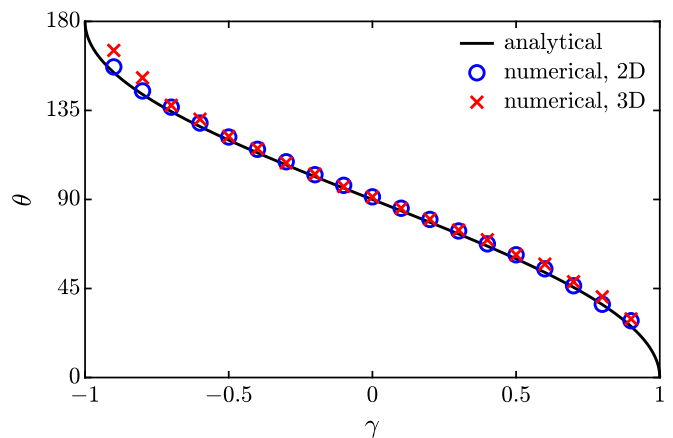


FIG. 10. Comparison of the contact angle obtained by the LB simulation of a static droplet on a curved surface with the analytical result derived from thermodynamic theory. The reduced temperature is  $T_r = 0.8$  and the liquid-vapor surface tension is  $\sigma_{lv} = 0.01$ . The liquid-vapor interface thickness is  $W_{lv} = 5$  for the three-dimensional numerical result for  $\gamma = -0.9$  and  $W_{lv} = 10$  for the other numerical results.

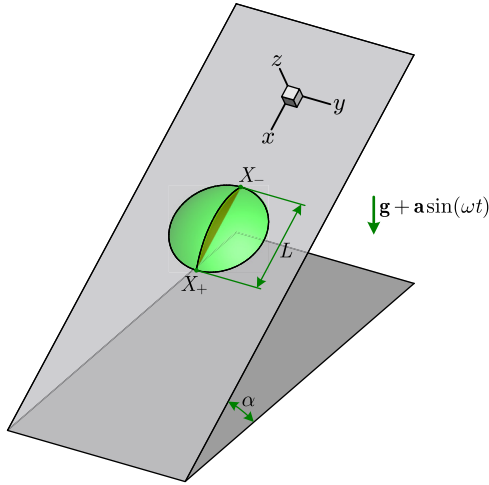


FIG. 11. Schematic of a moving droplet on an inclined wall with  $X_+$  and  $X_-$  the lowest and highest points of the three-phase contact line,  $L$  the droplet length defined as  $L = X_+ - X_-$ ,  $\alpha$  the angle between the wall and horizontal plane, and  $\mathbf{g}$  the gravitational acceleration. The coordinate system  $(x, y, z)^T$  is attached to the wall and an external acceleration  $\mathbf{a} \sin(\omega t)$  is applied to mimic the vertical and sinusoidal oscillation of the wall.

simulation, the coordinate system  $(x, y, z)^T$  is attached to the inclined wall and an external acceleration  $\mathbf{a} \sin(\omega t)$  is applied to mimic the vertical and sinusoidal oscillation of the wall, as illustrated by Fig. 11. The reduced temperature is set to  $T_r = 0.7$ , and the liquid-vapor surface tension and interface thickness are fixed at  $\sigma_{lv} = 0.01$  and  $W_{lv} = 10$ , respectively. The computational domain is chosen as  $896 \times 256 \times 128$ , where the solid surface is put on the lower side of the computational domain (i.e., the  $x$ - $y$  plane with  $z = 0$ ). The symmetric boundary condition is applied on the upper side of the computational domain (i.e., the  $x$ - $y$  plane with  $z = 128$ ), and periodic boundary conditions are applied in both the  $x$  and  $y$  directions, implying that the inclined wall is infinite in the  $x$  and  $y$  directions. The parameter  $\gamma$  in the EOS-dependent surface free-energy density is fixed at  $\gamma = \cos(\pi/4)$  to make the static contact angle  $\theta_0 = 45^\circ$ , and the wall inclination angle is set to  $\alpha = 30^\circ$ . The dimensionless relaxation time  $\tau$  is chosen as 0.6 to achieve a relatively low viscous dissipation.

To achieve an appropriate initialization of the moving droplet on the inclined wall, an auxiliary simulation of the droplet wetting process is first carried out with a hemispherical droplet deposited on the wall as follows:

$$\rho(\mathbf{x}, 0) = \frac{\rho_l + \rho_v}{2} - \frac{\rho_l - \rho_v}{2} \tanh \frac{|\mathbf{x} - \mathbf{x}_c| - r_0}{W_{lv}/\ln(19)}, \quad (40a)$$

$$\mathbf{u}(\mathbf{x}, 0) = \mathbf{0}, \quad (40b)$$

where  $\mathbf{x}_c = (0, 0, 0)^T$  and  $r_0 = 97.328$ . Note that the coordinate origin is placed at the center of the lower side of the computational domain, and the radius  $r_0$  is properly adjusted to make the droplet length after the wetting process precisely  $L_0 = 128$ . Here, the droplet length is defined as the distance between the lowest and highest points of the three-phase contact line as shown in Fig. 11. In the auxiliary simulation, the external force, including gravity and the one mimicking wall

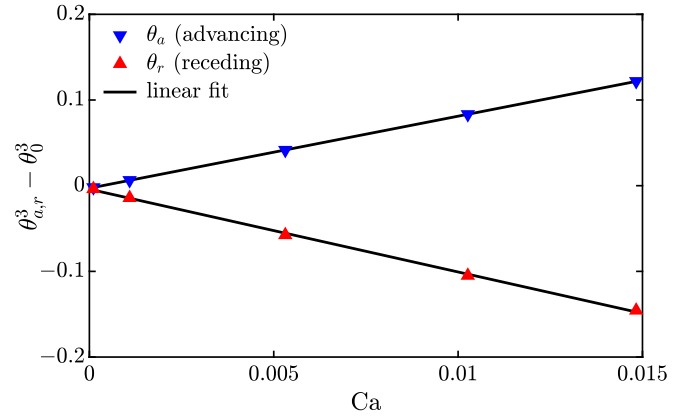


FIG. 12. Variations of the cubes of the dynamic contact angles (in radians) with the capillary number  $Ca$ , where  $\theta_a$  and  $\theta_r$  are the dynamic contact angles measured at the advancing and receding three-phase contact points in the symmetric midplane of the sliding droplet on the inclined wall, and  $\theta_0$  is the static contact angle measured when  $Ca = 0$ .

oscillation, is turned off, and thus a final static droplet on the inclined wall can be obtained, which is used as an appropriate initialization of the oscillating process. The external force is abruptly turned on at time  $t = 0$  in the oscillating process, and then the droplet starts moving on the inclined wall. To characterize this droplet-oscillating problem, and following the analytical work by Bradshaw and Billingham [52], three dimensionless parameters are introduced: the dimensionless oscillation strength  $\epsilon$ , the dimensionless oscillation frequency  $\hat{\omega}$ , and the dimensionless gravitational acceleration  $\hat{g}$ , which are defined as [27,52]

$$\epsilon = \frac{\rho_l |\mathbf{a}| L_0^2 \sin \alpha}{\sigma_{lv} \theta_0}, \quad \hat{\omega} = \omega \sqrt{\frac{\rho_l L_0^3}{\sigma_{lv} \theta_0}}, \quad \hat{g} = \frac{\rho_l |\mathbf{g}| L_0^2 \sin \alpha}{\sigma_{lv} \theta_0}, \quad (41)$$

where the static contact angle  $\theta_0$  should be in radians. Before proceeding further, the droplet sliding on a stationary wall is simulated to study the dynamic performance of the present multiphase LB model and its wetting condition treatment. The wall oscillation is not considered by setting the dimensionless oscillation strength  $\epsilon = 0$ . The droplet sliding is driven by gravity with the dimensionless gravitational acceleration  $\hat{g}$  being set to 0.04, 0.4, 2, 4, and 6. When the quasi-steady state of the sliding droplet is reached, the dynamic contact angles at the advancing and receding three-phase contact points in the symmetric midplane of the droplet, denoted by  $\theta_a$  and  $\theta_r$ , respectively, are measured and the capillary number, defined as  $Ca = \mu_l U_{cl} / \sigma_{lv}$ , is calculated. Here,  $\mu_l$  is the dynamic viscosity of the liquid phase and  $U_{cl}$  is the moving velocity of the three-phase contact line. The numerical results are shown in Fig. 12, where the Cox-Voinov law  $\theta_{a,r}^3 - \theta_0^3 \propto Ca$  is adopted for quantitative validation. Note that the static contact angle  $\theta_0$  here is measured when  $Ca = 0$  to avoid the numerical error of the wetting condition treatment. A good agreement between the numerical results and the Cox-Voinov law can be observed, which demonstrates the present model

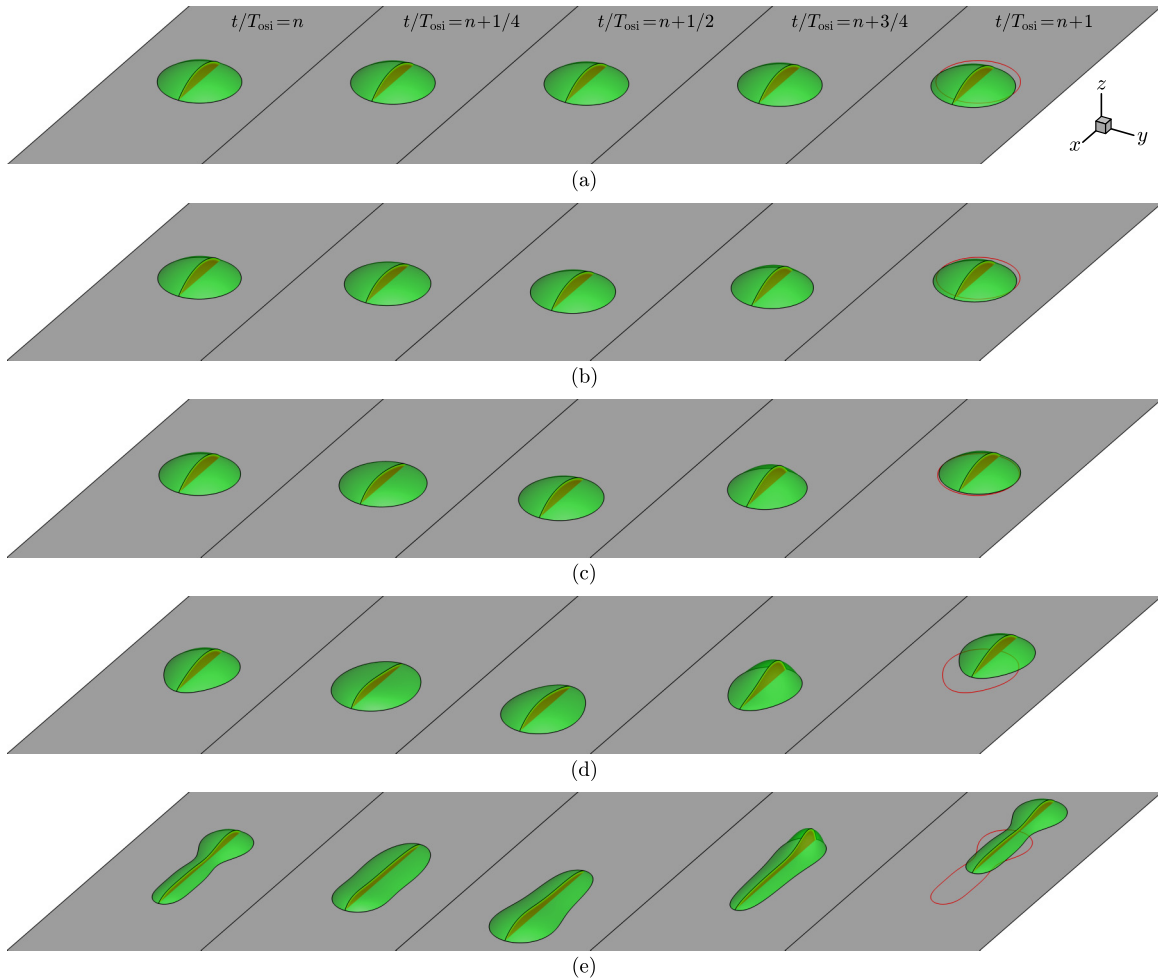


FIG. 13. Snapshots of the moving droplet on the inclined wall during the  $n$ th oscillation period for (a)  $\epsilon = 0$ , (b)  $\epsilon = 4$ , (c)  $\epsilon = 8$ , (d)  $\epsilon = 16$ , and (e)  $\epsilon = 32$ . The normalized times are  $t/T_{\text{osi}} = n, n + 1/4, n + 1/2, n + 3/4$ , and  $n + 1$  from the left to right panels, and the red solid line in the rightmost panel is the three-phase contact line in the leftmost panel.

and treatment can handle the dynamic contact line problems reasonably well.

In the following, the droplet moving on the oscillated wall is focused. The dimensionless oscillation frequency and gravitational acceleration are fixed at  $\hat{\omega} = 1.6$  and  $\hat{g} = 0.4$ , respectively. Figure 13 shows the snapshots of the moving droplet on the inclined wall during the  $n$ th oscillation period, where the dimensionless oscillation strength  $\epsilon$  is set to 0, 4, 8, 16, and 32 (corresponding to  $|\mathbf{a}| = 0, 1.071 \times 10^{-5}, 2.142 \times 10^{-5}, 4.283 \times 10^{-5}$ , and  $8.567 \times 10^{-5}$ , respectively, under the present configurations), and the time  $t$  is normalized by the oscillation period  $T_{\text{osi}} = 2\pi/\omega$ . Here,  $n = 10$  is chosen to avoid the effect of the abrupt turn-on of the external force at time  $t = 0$ . For  $\epsilon = 0$  which corresponds to a stationary wall, the droplet continuously slides down along the inclined wall due to gravity, as shown by Fig. 13(a). For  $\epsilon = 4, 8, 16$ , and 32 that correspond to an oscillated wall, the droplet slides down during the first half-period (i.e.,  $t/T_{\text{osi}} \in [n, n + 1/2]$ ) but climbs up during the second half-period (i.e.,  $t/T_{\text{osi}} \in [n + 1/2, n + 1]$ ), as shown by Figs. 13(b)–13(e). This is because the external acceleration  $\mathbf{a} \sin(\omega t)$  is in the same direction as the gravitational acceleration  $\mathbf{g}$  during the first half-period, but  $\mathbf{a} \sin(\omega t)$  is in the opposite direction of  $\mathbf{g}$  during the

second half-period and the magnitude of  $\mathbf{a}$  is much larger than that of  $\mathbf{g}$  as  $|\mathbf{a}|/|\mathbf{g}| = \epsilon/\hat{g} \gg 1$ . For  $\epsilon = 4$  corresponding to a very weak oscillation, the deformation of the droplet during one oscillation period is almost indistinguishable, and the net movement of the droplet within one oscillation period is sliding-down, as shown by Fig. 13(b). As  $\epsilon$  increases to 8 and 16, the wall oscillation becomes relatively strong, and the droplet deformation during one oscillation period is visually distinguishable. For  $\epsilon = 32$  corresponding to a very strong oscillation, the droplet is significantly stretched during the entire oscillation period. It can be seen from Figs. 13(c)–13(e) that the net movement of the droplet changes to climbing-up for  $\epsilon = 8, 16$ , and 32, and the net climbing-up distance increases as  $\epsilon$  increases. Figure 14 shows the movements of the lowest and highest points of the three-phase contact line during the time  $0 \leq t/T_{\text{osi}} \leq 10$ , where the coordinates of the lowest and highest points  $X_{\pm}$  are normalized by the initial droplet length  $L_0$ . For  $\epsilon = 0$ , the curves for  $X_{\pm}/L_0$  are linear and parallel to each other. For  $\epsilon = 4, 8, 16$ , and 32, the curves for  $X_{\pm}$  periodically oscillate with the same frequency as the wall oscillation, and their amplitudes increase as  $\epsilon$  increases. The results shown in Fig. 14 reconfirm that the net movement of the droplet is sliding-down for  $\epsilon = 0$  and 4, but changes to

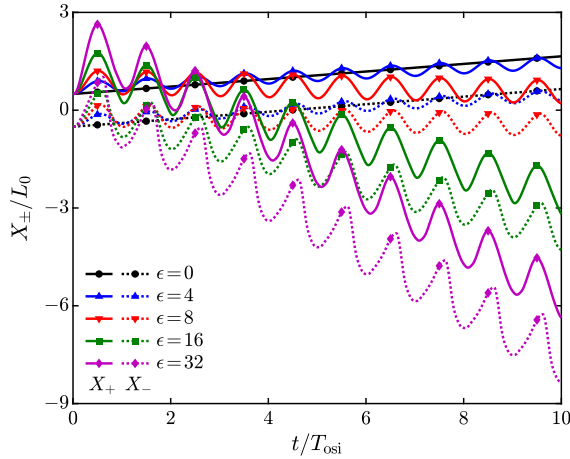


FIG. 14. Variations of the lowest and highest points of the three-phase contact line with the normalized time  $t/T_{\text{osi}}$  for  $\epsilon = 0, 4, 8, 16$ , and  $32$ , where the coordinates of the lowest and highest points  $X_{\pm}$  are normalized by the initial droplet length  $L_0$ .

climbing-up for  $\epsilon = 8, 16$ , and  $32$ . These droplet movement regimes captured by the present three-dimensional LB simulations are consistent with the experiments by Brunet *et al.* [53] and the two-dimensional LB simulations by Huang *et al.* [27].

Before closing this section, the overall velocity of the droplet, defined as  $U = S/T_{\text{osi}}$  and then normalized as  $U^* = UT_{\text{osi}}/L_0$ , is measured after 10 oscillation periods. Here,  $S$  is the net climbing-up distance within one oscillation period, and  $S < 0$  ( $U^* < 0$ ) and  $S > 0$  ( $U^* > 0$ ) correspond to the climbing-up and sliding-down regimes, respectively. For the sliding-down regime,  $\epsilon = 0, 2, 4$ , and  $6$  are considered. As for the climbing-up regime,  $\epsilon = 8, 12, 16, 20, 24, 28$ , and  $32$  are considered. According to our LB simulations, the critical dimensionless oscillation strength when the droplet remains static after one oscillation period (i.e., the droplet overall velocity  $U^* = 0$ ) is  $\epsilon_{\text{cr}} = 7.056$  for the situation with  $\hat{\omega} = 1.6$  and  $\hat{g} = 0.4$ . Figure 15 shows the variation of the droplet

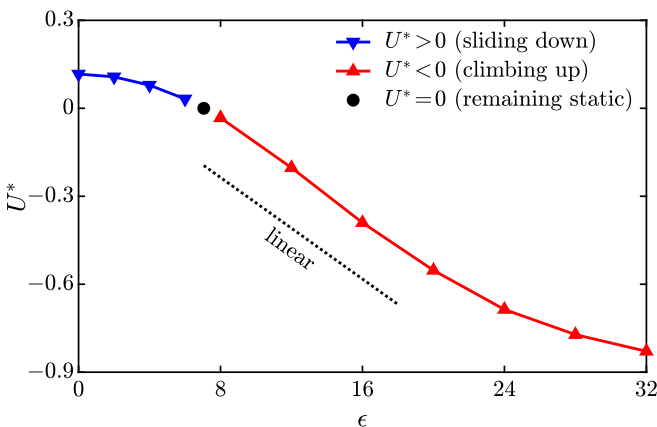


FIG. 15. Variation of the droplet overall velocity  $U^*$  with the dimensionless oscillation strength  $\epsilon$ , where the critical dimensionless oscillation strength when  $U^* = 0$  is  $\epsilon_{\text{cr}} = 7.056$  based on the LB simulations.

overall velocity with the dimensionless oscillation strength. It is interesting to note from the figure that  $U^*$  linearly varies with  $\epsilon$  in the climbing-up regime with a relatively small  $\epsilon$  ( $8 \leq \epsilon \leq 20$ ), while  $U^*$  nonlinearly varies with  $\epsilon$  in the sliding-down regime although  $\epsilon$  is much smaller ( $0 \leq \epsilon \leq 6$ ) for this regime. In the climbing-up regime with a relatively large  $\epsilon$  ( $20 \leq \epsilon \leq 32$ ), the increment of  $|U^*|$  gradually slows down as  $\epsilon$  increases, which can be explained by the larger deformation of the droplet and the stronger energy dissipation inside the droplet.

## V. CONCLUSION

In this work, the wettability of the liquid-vapor fluids on a solid surface is thermodynamically analyzed for a general multiphase EOS, and then an EOS-dependent surface free-energy density is proposed. With the present surface free-energy density, the fluid density on the solid surface is equal to the density in the bulk phase, and a simple closed-form analytical expression for the contact angle is derived. It is also found that the equilibrium condition thermodynamically derived with the present surface free-energy density is equivalent to the geometric formulation of the contact angle. The multiphase LB model with self-tuning EOS, strictly consistent with thermodynamic theory, is employed for the numerical validations, and the two-dimensional wetting condition treatment is extended to the three-dimensional situation with flat and curved surfaces. The contact angles obtained by the two- and three-dimensional LB simulations of static droplets on flat and curved surfaces agree well with the closed-form analytical expression, which validates the EOS-dependent surface free-energy density for wettability and the numerical method for multiphase flows (including the multiphase LB model with self-tuning EOS and its wetting condition treatment). Then, the three-dimensional LB simulation of a moving droplet on an inclined wall, which is vertically and sinusoidally oscillated, is carried out. The droplet slides down along the wall when the oscillation is relatively weak but climbs up against gravity when the oscillation is sufficiently strong. In the climbing-up regime, the droplet overall velocity  $U^*$  linearly varies with the dimensionless oscillation strength  $\epsilon$  when  $\epsilon$  is relatively small, but the increment of  $|U^*|$  gradually slows down as  $\epsilon$  increases when  $\epsilon$  is relatively large. In the sliding-down regime,  $U^*$  nonlinearly varies with  $\epsilon$  although  $\epsilon$  is much smaller for this regime.

## ACKNOWLEDGMENT

This work was supported by the National Natural Science Foundation of China through Grant No. 52006244.

## APPENDIX: OTHER EQUATIONS OF STATE

The van der Waals equation of state is given as [54]

$$p_{\text{EOS}} = \frac{\rho RT}{1 - b\rho} - a\rho^2, \quad (\text{A1a})$$

of which the indefinite integral can be calculated as

$$\Theta = \int p_{\text{EOS}} dv = -RT \ln \left( \frac{\rho}{1 - b\rho} \right) + a\rho. \quad (\text{A1b})$$

The coefficients  $a$  and  $b$  are related to the critical properties as follows:

$$a = \frac{9RT_{\text{cr}}}{8\rho_{\text{cr}}}, \quad b = \frac{1}{3\rho_{\text{cr}}}. \quad (\text{A1c})$$

The Redlich-Kwong equation of state is given as [55]

$$p_{\text{EOS}} = \frac{\rho RT}{1 - b\rho} - \frac{a\rho^2}{\sqrt{T}(1 + b\rho)}, \quad (\text{A2a})$$

of which the indefinite integral can be calculated as

$$\Theta = \int p_{\text{EOS}} dv = -RT \ln \left( \frac{\rho}{1 - b\rho} \right) + \frac{a}{b\sqrt{T}} \ln(1 + b\rho). \quad (\text{A2b})$$

The coefficients  $a$  and  $b$  are related to the critical properties as follows:

$$a = \frac{(1 + 2^{1/3} + 2^{2/3})RT_{\text{cr}}^{3/2}}{3\rho_{\text{cr}}}, \quad b = \frac{2^{1/3} - 1}{\rho_{\text{cr}}}. \quad (\text{A2c})$$

The Redlich-Kwong-Soave equation of state is given as [56]

$$p_{\text{EOS}} = \frac{\rho RT}{1 - b\rho} - \frac{\alpha a \rho^2}{1 + b\rho}, \quad (\text{A3a})$$

of which the indefinite integral can be calculated as

$$\Theta = \int p_{\text{EOS}} dv = -RT \ln \left( \frac{\rho}{1 - b\rho} \right) + \frac{\alpha a}{b} \ln(1 + b\rho). \quad (\text{A3b})$$

Here,  $\alpha$  is a function of the reduced temperature  $\alpha(T_r) = [1 + (0.480 + 1.574\omega - 0.176\omega^2)(1 - \sqrt{T_r})]^2$  with  $\omega$  the acentric factor. The coefficients  $a$  and  $b$  are related to the critical properties as follows:

$$a = \frac{(1 + 2^{1/3} + 2^{2/3})RT_{\text{cr}}}{3\rho_{\text{cr}}}, \quad b = \frac{2^{1/3} - 1}{\rho_{\text{cr}}}. \quad (\text{A3c})$$

The Peng-Robinson equation of state is given as [57]

$$p_{\text{EOS}} = \frac{\rho RT}{1 - b\rho} - \frac{\alpha a \rho^2}{1 + 2b\rho - (b\rho)^2}, \quad (\text{A4a})$$

of which the indefinite integral can be calculated as

$$\Theta = \int p_{\text{EOS}} dv = -RT \ln \left( \frac{\rho}{1 - b\rho} \right) + \frac{\alpha a}{\sqrt{2}b} \operatorname{arctanh} \left( -\frac{1 - b\rho}{\sqrt{2}} \right). \quad (\text{A4b})$$

Here,  $\alpha$  is a function of the reduced temperature  $\alpha(T_r) = [1 + (0.37464 + 1.54226\omega - 0.26992\omega^2)(1 - \sqrt{T_r})]^2$  with  $\omega$  the acentric factor, and  $\operatorname{arctanh}x = \frac{1}{2} \ln \left( \frac{1+x}{1-x} \right)$  denotes the inverse hyperbolic tangent function. The coefficients  $a$  and  $b$  are related to the critical properties as follows:

$$a = \frac{2^{2/3}(4 + 3\sqrt{2})^{1/3}(20 + 45\sqrt{2}) + 2^{1/3}(190 + 120\sqrt{2}) - 34(4 + 3\sqrt{2})^{2/3}}{96(4 + 3\sqrt{2})^{2/3}} \frac{RT_{\text{cr}}}{\rho_{\text{cr}}},$$

$$b = \frac{2^{1/3}(4 + 3\sqrt{2})^{2/3} - (4 + 3\sqrt{2})^{1/3} - 2^{2/3}}{3(4 + 3\sqrt{2})^{1/3}} \frac{1}{\rho_{\text{cr}}}. \quad (\text{A4c})$$

At last, it is worth pointing out that the scaling factor  $K_{\text{EOS}}$  should also be introduced into the above EOSs when they are incorporated into the multiphase LB model with self-tuning EOS [see Eq. (29)]. The way to incorporate these EOSs (i.e., the corresponding interaction strength  $G$  and lattice sound speed  $c_s$ ) can be found in Ref. [58].

- 
- [1] A. K. Gunstensen, D. H. Rothman, S. Zaleski, and G. Zanetti, Lattice Boltzmann model of immiscible fluids, *Phys. Rev. A* **43**, 4320 (1991).
- [2] X. Shan and H. Chen, Lattice Boltzmann model for simulating flows with multiple phases and components, *Phys. Rev. E* **47**, 1815 (1993).
- [3] M. R. Swift, W. R. Osborn, and J. M. Yeomans, Lattice Boltzmann Simulation of Nonideal Fluids, *Phys. Rev. Lett.* **75**, 830 (1995).
- [4] H. Huang, M. C. Sukop, and X.-Y. Lu, *Multiphase Lattice Boltzmann Methods: Theory and Application* (Wiley-Blackwell, Oxford, UK, 2015).
- [5] Q. Li, K. H. Luo, Q. J. Kang, Y. L. He, Q. Chen, and Q. Liu, Lattice Boltzmann methods for multiphase flow and phase-change heat transfer, *Prog. Energy Combust. Sci.* **52**, 62 (2016).
- [6] R. Huang, H. Wu, and N. A. Adams, Mesoscopic Lattice Boltzmann Modeling of the Liquid-Vapor Phase Transition, *Phys. Rev. Lett.* **126**, 244501 (2021).
- [7] J. S. Rowlinson and B. Widom, *Molecular Theory of Capillarity* (Oxford University Press, Oxford, UK, 1982).
- [8] M. Sbragaglia, K. Sugiyama, and L. Biferale, Wetting failure and contact line dynamics in a Couette flow, *J. Fluid Mech.* **614**, 471 (2008).
- [9] P. G. de Gennes, Wetting: Statics and dynamics, *Rev. Mod. Phys.* **57**, 827 (1985).
- [10] X. Shan, Analysis and reduction of the spurious current in a class of multiphase lattice Boltzmann models, *Phys. Rev. E* **73**, 047701 (2006).
- [11] M. Sbragaglia, R. Benzi, L. Biferale, S. Succi, K. Sugiyama, and F. Toschi, Generalized lattice Boltzmann method with multirange pseudopotential, *Phys. Rev. E* **75**, 026702 (2007).

- [12] Q. Li, K. H. Luo, and X. J. Li, Forcing scheme in pseudopotential lattice Boltzmann model for multiphase flows, *Phys. Rev. E* **86**, 016709 (2012).
- [13] T. Inamuro, N. Konishi, and F. Ogino, A Galilean invariant model of the lattice Boltzmann method for multiphase fluid flows using free-energy approach, *Comput. Phys. Commun.* **129**, 32 (2000).
- [14] A. Mazloomi M, S. S. Chikatamarla, and I. V. Karlin, Entropic Lattice Boltzmann Method for Multiphase Flows, *Phys. Rev. Lett.* **114**, 174502 (2015).
- [15] Z. Guo, Well-balanced lattice Boltzmann model for two-phase systems, *Phys. Fluids* **33**, 031709 (2021).
- [16] R. Huang, H. Wu, and N. A. Adams, Lattice Boltzmann model with self-tuning equation of state for multiphase flows, *Phys. Rev. E* **99**, 023303 (2019).
- [17] X. He and G. D. Doolen, Thermodynamic foundations of kinetic theory and lattice Boltzmann models for multiphase flows, *J. Stat. Phys.* **107**, 309 (2002).
- [18] P. Raiskinmäki, A. Shakib-Manesh, A. Jäsberg, A. Koponen, J. Merikoski, and J. Timonen, Lattice-Boltzmann simulation of capillary rise dynamics, *J. Stat. Phys.* **107**, 143 (2002).
- [19] R. Benzi, L. Biferale, M. Sbragaglia, S. Succi, and F. Toschi, Mesoscopic modeling of a two-phase flow in the presence of boundaries: The contact angle, *Phys. Rev. E* **74**, 021509 (2006).
- [20] C. E. Colosqui, M. E. Kavousanakis, A. G. Papanthasiou, and I. G. Kevrekidis, Mesoscopic model for microscale hydrodynamics and interfacial phenomena: Slip, films, and contact-angle hysteresis, *Phys. Rev. E* **87**, 013302 (2013).
- [21] Q. Li, Y. Yu, and K. H. Luo, Implementation of contact angles in pseudopotential lattice Boltzmann simulations with curved boundaries, *Phys. Rev. E* **100**, 053313 (2019).
- [22] X. Shan and H. Chen, Simulation of nonideal gases and liquid-gas phase transitions by the lattice Boltzmann equation, *Phys. Rev. E* **49**, 2941 (1994).
- [23] A. J. Briant, P. Papatzacos, and J. M. Yeomans, Lattice Boltzmann simulations of contact line motion in a liquid-gas system, *Phil. Trans. R. Soc. Lond. A* **360**, 485 (2002).
- [24] A. J. Briant, A. J. Wagner, and J. M. Yeomans, Lattice Boltzmann simulations of contact line motion. I. Liquid-gas systems, *Phys. Rev. E* **69**, 031602 (2004).
- [25] J. W. Cahn, Critical point wetting, *J. Chem. Phys.* **66**, 3667 (1977).
- [26] C. Semperebon, T. Krüger, and H. Kusumaatmaja, Ternary free-energy lattice Boltzmann model with tunable surface tensions and contact angles, *Phys. Rev. E* **93**, 033305 (2016).
- [27] R. Huang, Q. Li, and N. A. Adams, Surface thermodynamics and wetting condition in the multiphase lattice Boltzmann model with self-tuning equation of state, *J. Fluid Mech.* **940**, A46 (2022).
- [28] A. J. Wagner, Thermodynamic consistency of liquid-gas lattice Boltzmann simulations, *Phys. Rev. E* **74**, 056703 (2006).
- [29] L.-Q. Chen, Chemical potential and Gibbs free energy, *MRS Bull.* **44**, 520 (2019).
- [30] R. Huang, Mesoscopic perspectives on dynamic van der Waals theory for liquid-vapor phase transition, *Phys. Fluids* **34**, 121704 (2022).
- [31] D. J. Korteweg, Sur la forme que prennent les équations du mouvements des fluides si l'on tient compte des forces capillaires causées par des variations de densité considérables mais connues et sur la théorie de la capillarité dans l'hypothèse d'une variation continue de la densité, *Arch. Néerl. Sci. Exactes Nat.* **6**, 1 (1901).
- [32] T. Krüger, H. Kusumaatmaja, A. Kuzmin, O. Shardt, G. Silva, and E. M. Viggien, *The Lattice Boltzmann Method: Principles and Practice* (Springer, Cham, 2017).
- [33] K. Connington and T. Lee, Lattice Boltzmann simulations of forced wetting transitions of drops on superhydrophobic surfaces, *J. Comput. Phys.* **250**, 601 (2013).
- [34] K. W. Connington, T. Lee, and J. F. Morris, Interaction of fluid interfaces with immersed solid particles using the lattice Boltzmann method for liquid-gas-particle systems, *J. Comput. Phys.* **283**, 453 (2015).
- [35] A. Fakhari and D. Bolster, Diffuse interface modeling of three-phase contact line dynamics on curved boundaries: A lattice Boltzmann model for large density and viscosity ratios, *J. Comput. Phys.* **334**, 620 (2017).
- [36] Q. He, Y. Li, W. Huang, Y. Hu, and Y. Wang, Lattice Boltzmann model for ternary fluids with solid particles, *Phys. Rev. E* **101**, 033307 (2020).
- [37] X. Zhang, H. Liu, and J. Zhang, A new capillary force model implemented in lattice Boltzmann method for gas-liquid-solid three-phase flows, *Phys. Fluids* **32**, 103301 (2020).
- [38] P. Yue, Thermodynamically consistent phase-field modelling of contact angle hysteresis, *J. Fluid Mech.* **899**, A15 (2020).
- [39] R. C. Tolman, The effect of droplet size on surface tension, *J. Chem. Phys.* **17**, 333 (1949).
- [40] M. Lulli, L. Biferale, G. Falcucci, M. Sbragaglia, and X. Shan, Mesoscale perspective on the Tolman length, *Phys. Rev. E* **105**, 015301 (2022).
- [41] S. A. Hosseini, B. Dorschner, and I. V. Karlin, Towards a consistent lattice Boltzmann model for two-phase fluids, *J. Fluid Mech.* **953**, A4 (2022).
- [42] M. Lulli, L. Biferale, G. Falcucci, M. Sbragaglia, and X. Shan, Mesoscale modelling of the Tolman length in multi-component systems, in *From Kinetic Theory to Turbulence Modeling: The Legacy of Carlo Cercignani* (edited by P. Barbante, F. D. Belgiorio, S. Lorenzani, L. Valdetaro) (Springer, Singapore, 2023).
- [43] S. Gong, F. Hong, Q. Guo, L. Zhang, and P. Cheng, Mesoscopic approach for nanoscale liquid-vapor interfacial statics and dynamics, *Int. J. Heat Mass Tran.* **194**, 123104 (2022).
- [44] H. Ding and P. D. M. Spelt, Wetting condition in diffuse interface simulations of contact line motion, *Phys. Rev. E* **75**, 046708 (2007).
- [45] R. Huang, Q. Li, and Y. Qiu, Three-dimensional lattice Boltzmann model with self-tuning equation of state for multiphase flows, to be published.
- [46] R. Huang and H. Wu, Third-order analysis of pseudopotential lattice Boltzmann model for multiphase flow, *J. Comput. Phys.* **327**, 121 (2016).
- [47] R. Huang, H. Wu, and N. A. Adams, Density gradient calculation in a class of multiphase lattice Boltzmann models, *Phys. Rev. E* **100**, 043306 (2019).
- [48] R. Huang, L. Lan, and Q. Li, Lattice Boltzmann simulations of thermal flows beyond the Boussinesq and ideal-gas approximations, *Phys. Rev. E* **102**, 043304 (2020).
- [49] R. Huang, H. Wu, and N. A. Adams, Eliminating cubic terms in the pseudopotential lattice Boltzmann model for multiphase flow, *Phys. Rev. E* **97**, 053308 (2018).

- [50] N. F. Carnahan and K. E. Starling, Equation of state for nonattracting rigid spheres, *J. Chem. Phys.* **51**, 635 (1969).
- [51] R. Huang, H. Wu, and N. A. Adams, Lattice Boltzmann model with adjustable equation of state for coupled thermohydrodynamic flows, *J. Comput. Phys.* **392**, 227 (2019).
- [52] J. T. Bradshaw and J. Billingham, Thick drops climbing uphill on an oscillating substrate, *J. Fluid Mech.* **840**, 131 (2018).
- [53] P. Brunet, J. Eggers, and R. D. Deegan, Vibration-Induced Climbing of Drops, *Phys. Rev. Lett.* **99**, 144501 (2007).
- [54] J. D. van der Waals, *On the Continuity of the Gaseous and Liquid States*, edited by J. S. Rowlinson (Dover, New York, NY, 2004).
- [55] O. Redlich and J. N. S. Kwong, On the thermodynamics of solutions. V. An equation of state. Fugacities of gaseous solutions, *Chem. Rev.* **44**, 233 (1949).
- [56] G. Soave, Equilibrium constants from a modified Redlich-Kwong equation of state, *Chem. Eng. Sci.* **27**, 1197 (1972).
- [57] D.-Y. Peng and D. B. Robinson, A new two-constant equation of state, *Ind. Eng. Chem. Fund.* **15**, 59 (1976).
- [58] Q. Li, Y. Xing, and R. Huang, Equations of state in multiphase lattice Boltzmann method revisited, *Phys. Rev. E* **107**, 015301 (2023).